



Distribution and origin of submarine landslides in the active margin of the southern Alboran Sea (Western Mediterranean Sea)

E. d'Acremont, Sara Lafuerza, Alain Rabaute, M. Lafosse, M. Jollivet Castelot, Christian Gorini, B. Alonso, G. Ercilla, J.T. Vazquez, T. Vandorpe, et al.

► To cite this version:

E. d'Acremont, Sara Lafuerza, Alain Rabaute, M. Lafosse, M. Jollivet Castelot, et al.. Distribution and origin of submarine landslides in the active margin of the southern Alboran Sea (Western Mediterranean Sea). *Marine Geology*, 2022, 445, pp.106739. 10.1016/j.margeo.2022.106739 . hal-03610750

HAL Id: hal-03610750

<https://hal.science/hal-03610750>

Submitted on 16 Mar 2022

HAL is a multi-disciplinary open access archive for the deposit and dissemination of scientific research documents, whether they are published or not. The documents may come from teaching and research institutions in France or abroad, or from public or private research centers.

L'archive ouverte pluridisciplinaire **HAL**, est destinée au dépôt et à la diffusion de documents scientifiques de niveau recherche, publiés ou non, émanant des établissements d'enseignement et de recherche français ou étrangers, des laboratoires publics ou privés.

Distribution and origin of submarine landslides in the active margin of the southern Alboran Sea (Western Mediterranean Sea)

d'Acremont E.¹; Lafuerza S.¹; Rabaute A.¹; Lafosse M.¹; Jollivet Castelot M.¹; Gorini C.¹
Alonso B.²; Ercilla G.²; Vazquez J.T.³; Vandorpe T.^{4,5}; Juan C.^{2,6}; Migeon S.⁷; Ceramicola S.⁸; Lopez-
Gonzalez N.³; Rodriguez M.⁹; El Moumni B.¹⁰; Benmarha O.¹¹; Ammar A.¹¹

¹Sorbonne Université, CNRS-INSU, Institut des Sciences de la Terre Paris, IStEP, F-75005 Paris, France

²Instituto de Ciencias del Mar, CSIC, 08003 Barcelona, Spain

³Instituto Español de Oceanografía (IEO), C.O. Málaga, 29640 Fuengirola, Málaga, Spain

⁴Flanders Marine Institute (VLIZ), Wandelaarkaai 7, 8400, Oostende, Belgium

⁵Department of Geology, Ghent University, Krijgslaan 281 S8, 9000, Gent, Belgium

⁶Instituto Español de Oceanografía (IEO), C.O. Cádiz, 11006 Cádiz, Spain

⁷Géoazur, Université de Nice-Sophia Antipolis-CNRS-OCA, France

⁸National Institute of Oceanography and Applied Geophysics - OGS, 34010, Sgonico, TS, Italy

⁹Laboratoire de Géologie, Ecole normale supérieure, PSL research university, CNRS UMR 8538, 24 rue Lhomond, 75005 Paris, France

¹⁰Université Abdelmalek Essaadi, Morocco

¹¹Université Mohammed V-Agdal, Rabat, Morocco

Abstract

Earthquakes are the most commonly cited cause of offshore slope failure, followed by high sedimentation rates and ensuing pore pressure build-up. In the South Alboran Sea, the moderate seismicity ($M_w=6.4$) of the strike-slip Al Idrissi Fault Zone does not appear to control directly the landslides distribution. To provide a preliminary geohazard assessment, we characterized the spatial distribution, the volume and the ages of the submarine landslides from multibeam and seismic reflection data in the southern part of the Alboran Sea. Since the Quaternary numerous submarine landslide processes have affected the marine sedimentary cover with volumes of the mass transport deposits (MTD) estimated between 0.01 and 15 km³. West of the Al Idrissi Fault Zone, along the South Alboran Ridge's northern flank, the distribution of the MTD follows the SW-NE bank and ridge trend that correlates with blind thrusts and folds covered by a plastered contourite drift. A pockmark field, related to fluid escape, is visible near landslide scars where the contourite drift is relatively thicker. In this area, landslide scars occur on variable slopes (2-24°) and their associated MTDs show variable decompacted volumes (0.01-10 km³). East of the Al Idrissi Fault Zone, between the Alboran Ridge and

the Pytheas Bank, the mapped MTDs have uneven volume. The smaller ones ($<1 \text{ km}^3$) have their slide scars on steep slopes ($>10^\circ$), whereas those of the largest ones ($3\text{-}15 \text{ km}^3$) occur on gentler slopes ($<5^\circ$). These observations and a slope stability analysis suggest that the combination of seismic shaking, blind thrusts activity, relatively high sedimentation rate of contourite deposits with potential weak layers, and fluid escape dynamics are likely the main controlling mechanisms. These causal factors would explain the concentration of landslide head scarps at the edge of the thickest parts of the contourite drifts (i.e. crest). Slides may have been controlled locally by fluid overpressures in line with blind thrusts. Additionally, low to moderate seismicity potentially triggered by nearby faults might regionally have played a role in destabilising the landslides since 1.12 Ma (Q2 unit), which coincides with the propagation of the Al Idrissi Fault Zone in the southern Alboran Sea.

1 Introduction

Submarine landslides, encompassing all forms of submarine slope failures, may translate into the destruction of seabed infrastructures and coastal areas' collapse into the sea. They can mobilize up to thousands of km^3 of seafloor material (e.g. Storegga Slide, 8200 years ago; Haflidason et al., 2004; Calvès et al., 2015), volumes that are substantially larger than their subaerial counterparts (Dussauge et al., 2003; Urgeles and Camerlenghi, 2013). Mobilization of seafloor volumes may trigger tsunamis (e.g., Papua-New Guinea in 1998, Tappin et al. 2001) and submarine cable breaks (e.g., Taiwan in 2006, Marle, 2007; Carter et al., 2014).

Mediterranean coasts have a history of tsunamis caused by submarine landslides (Nice in 1979, Dan et al., 2007; Gioia Tauro in 1977, Colantoni et al., 1992; Stromboli in 2002, Chiocci et al., 2008; among others). Earthquakes can generate submarine landslides and tsunamis (Messina in 1908, Valensise and Pantosti, 1992; Amorgos in 1956, Okal et al., 2009; Gioia Tauro landslides in 1977, Zaniboni et al. 2014; Boumerdès in 2003, Alasset et al., 2006; Cattaneo et al., 2012). A recent event of earthquakes generating submarine landslide and tsunami has recently been documented on the Samos Island and Izmir coast (October 2020; Triantafyllou et al., 2021). In the southern part of the Alboran Sea, two studies, the $\sim 1 \text{ km}^3$ Alborani (Macías et al., 2015) and the $\sim 2 \text{ km}^3$ Xauen (Rodriguez et al., 2017) submarine slides, model the tsunamigenic potential at the Moroccan coastline and suggest local run-ups in the order of 1 m. These results illustrate that small submarine landslides would flood densely populated coastal cities in Spain and Morocco, demonstrating a regional geohazard. These examples illustrate that offshore landslides represent an important risk for the Mediterranean coastal communities, industry, and offshore infrastructure. The Spanish and Moroccan Mediterranean coasts

hold several environmentally protected areas (UNEP/MAP, 2015), important maritime transport routes, and have great potential for aquaculture zones (e.g., in the Al Hoceima area, Nada et al., 2018). The increasing number of infrastructures and population (expected to grow by 75% by 2025, UNEP/MAP/MED POL 2012) make the assessments of submarine landslide geohazards a key condition for their safe and sustainable development.

In the Alboran basin, tectonics, deep water currents and sea-level changes shaped the seafloor into its present-day topographic complexity with structural highs and depressions enclosed within a relatively small area ($\sim 50\,000\text{ km}^2$) (e.g. Ercilla et al., 2016; Estrada et al., 2018) (Fig. 1). Seafloor observations show the occurrence of landslides that have been related to seismic faults (Estrada et al., 2018; Galindo-Zaldivar et al., 2018), fluid dynamics and contourite deposition (Somoza et al., 2012). Most of the recent seismicity (e.g., Gracia et al., 2019) concentrates along the NNE-SSW Al Idrissi Fault Zone (AIFZ), which crosses the whole basin. In line with the seismogenic AIFZ, earthquake shaking could be considered as the main potential triggering mechanism of slope failures (Galindo-Zaldivar et al., 2018). However landslides are scarce in the most active area (Figs 2A, B) and localize far from the Al Idrissi seismogenic zone merely along a NE-SW E-W folds and faults belt called the Alboran Ridge and the South Alboran ridge (Fig. 1, AR and SAR respectively; Lafosse et al., 2020).

Sediment core studies reveal large variability in texture and geotechnical properties in the Alboran Basin with strong variability in the grain size of the contourite deposits (Baraza et al., 1992; Ercilla et al., 2021). Stability analysis suggests that the sediment is stable under static gravitational loading but potentially unstable under seismic loading (Baraza et al., 1992).

Except in the northern part of the Alboran Basin (Casas et al., 2011; Alonso et al., 2014), most of the submarine landslides' geometries and chronologies are yet to be described, and their causal factors still remain poorly known. The triggering and preconditioning factors causing the submarine landslide spatial distribution is still unresolved (Fig. 2A, B).

To provide a preliminary geohazard assessment, we characterized the spatial distribution, the volume and the ages of the submarine landslides from multibeam and seismic reflection data in the southern part of the Alboran Sea. We focus the discussion on the triggering and preconditioning factors, in particular with regards to slope steepness, fluid escapes, tectonic features and earthquakes by performing morpho-structural and slope stability analysis. Our data reveal that submarine landslides occurred repetitively throughout the Quaternary, notably after a tectonic reorganization of the Alboran Basin from 1.12 Ma.

2 Geological setting

The Alboran Sea was formed due to westward Tethyan slab retreat (Calvert et al., 2000; Jolivet et al., 2008; Platt et al., 2003; Spakman and Wortel, 2004; Do Couto et al., 2016; d'Acremont et al. 2020) within a compressive context of the African-European convergence since the end of the Oligocene (Comas et al., 1999; Gutscher et al., 2002; Jolivet et al., 2009; Mauffret et al., 2007; Mauffret et al., 1992). Above the metamorphic and volcanic basement, a thick Miocene depocenter is located in the western basin where mud volcanoes and other shale tectonic processes affect the seafloor (Fig. 1) (Pérez-Belzuz et al., 1997; Comas et al., 1999).

From the Tortonian onward, compressive tectonics reactivated extensional and strike-slip structures (Estrada et al., 1997; Martínez García et al., 2017; d'Acremont et al., 2020). Since the start of this tectonic inversion, 9 Ma ago, the topographic highs directed the water masses circulation and the location and geometry of contouritic systems (Juan et al., 2016; Lafosse et al., 2020; d'Acremont et al. 2020). Since 5.33 Ma and the end of the Messinian Salinity Crisis, the interaction between tectonic activity (i.e. thrust and fold growths, seismicity) and the formation of contourite systems and seamounts explain the morphological features of the seafloor (Figs 1 and 3) (Juan et al. 2016; 2020). Contourite drifts such as the 650 m thick Ceuta drift (Fig. 1) are building up in the southern Alboran Sea due to the interaction of the Dense Mediterranean Waters (DMW Fig. 1; which comprise the lower Tyrrhenian Dense Waters and Western Mediterranean Deep Waters), that accelerates toward the Strait of Gibraltar, and of the Modified Atlantic Water current (AW Fig. 1; Ercilla et al., 2015; Juan et al., 2016; Ercilla et al., 2019). Contourite systems formed when the Gibraltar Strait opened (Ercilla et al. 2002, Juan et al. 2016). In response to the continuous influence of Mediterranean water masses after the opening of the Strait of Gibraltar (Juan et al., 2016), contourite drifts (plastered, sheeted, elongated, separated, and confined mottled drifts) and associated erosive features (terraces, scarps, moats, and channels) mainly constitute the Pliocene-Quaternary sedimentary record. About 2.6 Ma ago, the surficial Atlantic waters and the deeper and dense Mediterranean waters favoured the erosion and the sediment accumulation in all Spanish and Moroccan margins and adjacent margins of the Alboran Sea (Juan et al., 2016). Contourite deposits built-up synchronously with the growth of thrusts, folds, mud diapirs and volcanoes, which led to important accumulation of sediments on slopes and basins (Pérez-Belzuz et al., 1997; Somoza et al., 2012; Ercilla et al., 2015; Juan et al., 2016). The plastered drifts dominate the Spanish and Moroccan continental slopes whereas sheeted drifts dominate the sub-basins (Juan et al. 2016; 2020). Along the Moroccan margin, the Ceuta drift (Fig. 1) is mainly composed of muds with intercalated layers (50 cm) of sandy muds, bounded by sharp surfaces and silty clay layers (Ercilla et al., 2002).

Strike-slip and reverse faults accommodated the convergence between the Eurasian and African plates (Gràcia et al., 2019; d'Acremont et al. 2020; Estrada et al., 2021). In the southern part of the Alboran basin, thrusts and folds form large E-W to NE-SW prominent morpho-structural highs (Fig. 2B). The

Xauen-Tofiño Banks and Francesc Pagès Seamount form the South Alboran compressive Ridge above the thick Miocene shales (called SAR; d'Acremont et al. 2020; Lafosse et al. 2020). North of the SAR, three blind thrusts limit the front of the compressional deformation (d'Acremont et al. 2020; Lafosse et al. 2020; called DF1, DF2, and DF3 in Figs 2B and 3B). Recent deformations are related to the growth of the anticline related to these blind thrust activities (d'Acremont et al. 2020). Eastward, the Alboran Ridge is a compressive structure with blind thrusts, accommodating the African plate indentation in the Alboran block (Figs 1 and 2A; Martínez-García et al., 2017, Estrada et al., 2018). Compared to the SAR, the Alboran Ridge is narrower and is characterized by steeper slopes (Fig. 3). The AIFZ (Gracia et al., 2019; d'Acremont et al., 2020; Lafosse et al., 2020; Figs 1 and 2) crosses these structures and extends over the Alboran basin from southern Spain (Campo de Dalías/Adra region) to Morocco (Al Hoceima area; d'Acremont et al. 2014; Lafosse et al. 2020) (Figs 1 and 2). The AIFZ is a Quaternary NNE-SSW sinistral strike-slip structure (Gràcia et al., 2019; Lafosse et al., 2016, 2020), conjugated with NW-SE dextral faults toward the northern tip of the Alboran Ridge (Yusuf Fault and Averroes Fault Estrada et al., 2021; Fig 1). Most of the seismicity in the Alboran Basin is concentrated along this NNE-SSW AIFZ (Fig. 2A; Grevemeyer et al., 2015; Gracia et al., 2019; Stich et al., 2020). In southern Spain, the Adra 1910 earthquake has been estimated up to magnitude $M_w = 6.1$ (Stich et al., 2003), while in Northern Morocco, the Al Hoceima area has been affected by three recent seismic events (earthquakes, Fig. 1): May 26, 1994 ($M_w = 5.6$), February 21, 2004 ($M_w = 6.4$), January 25, 2016 ($M_w = 6.4$), (Medina and Cherkaoui, 2017; Galindo-Zaldívar et al., 2018; Kariche et al., 2018; Gràcia et al., 2019). The February 21, 2004 event yielded 628 casualties (Stich et al., 2005). These earthquakes are located along the AIFZ or related segments. Historical earthquakes are also described with intensities between VIII and X (MSK Intensity; Peláez et al., 2007; Palano et al., 2015). Long recurrence periods are suggested for these large earthquakes, due to the low plate convergence velocity (>1 000 years, Gràcia et al., 2019).

3 Data and methods

3.1 Geophysical dataset

Two key areas, located west and east of the AIFZ, are investigated: the northern flank of the Xauen-Tofiño banks and Francesc Pagès Seamount (SAR region); and the South Alboran Basin confined between the Alboran Ridge and the Pytheas Bank (SAB region; Figs 1 and 2). The dataset includes swath-bathymetry and sub-bottom/seismic reflection profiles acquired during academic oceanographic campaigns CONTOURIBER (2010), Marlboro-1 (2011), Marlboro-2 (2012), SARAS (2012), MONTERA (2012), and INCRISIS (2016) (Fig. 2C). The multibeam datasets were compiled into a

25 m resolution bathymetric map for the area of interest. Multibeam data were processed with the Ifremer CARAIBES and QPS QINSy softwares. High- and very high-resolution seismic reflection data were used for the geomorphological and stratigraphic interpretations. The seismic data originate from a multi-channel airgun system yielding 5 m and 10 m vertical resolution from academic and industrial acquisitions respectively, a single-channel SIG sparker system with 1 m of vertical resolution, and a TOPAS full ocean depth hull-mounted parametric echosounder system of decimetric vertical resolution (Fig. 2C).

3.2 Chronostratigraphy

The relative chronostratigraphy of submarine landslides is taken from the seismic stratigraphy of Juan et al. (2016) following the correlation of ODP Sites 976 and 979 with seismic reflection profiles (Figs 2C and 4). The following nine regional stratigraphic horizons are identified on the available seismic reflection lines from the Messinian to late Quaternary (Fig. 4):

- Top Messinian and base Pliocene horizon: M (5.33 Ma).
- Intra-Pliocene horizons: P0 (4.5 Ma) and P1 (3.3 Ma).
- Base Quaternary horizon: BQD (2.6 Ma).
- Intra-Quaternary horizons: Q0 (1.8 Ma), Q1 (1.12 Ma), Q2 (0.7 Ma), MIS12 and MIS8 horizons.

Between these horizons, up to seven stratigraphic units (PL1 to PL3 and QT1 to QT4) were distinguished (Juan et al. 2016; Fig. 4). Based on this chronostratigraphy obtained after correlation of ODP data and available seismic data (Juan et al., 2016), we can approximate when the submarine landslides were triggered (Fig. 4).

3.3 Landslides: terminology, characterization and classification

The term landslide encompasses the displacement of sediment and involves different types of processes, from slides and slumps to gravity currents or mass-flows (Hampton et al., 1996; Locat and Lee, 2002). Scars, evacuation areas, deposits are typically associated to a submarine landslide (Hampton et al., 1996). Their deposits are named Mass Transport Deposit (MTD; Hampton et al., 1996). In this study, we recognize MTDs from their seismic facies and their topography in the bathymetry. Multibeam bathymetry and seismic reflection data are essential tools for identifying and characterizing submarine landslides (McAdoo et al., 2000; Principaud et al., 2015; Clare et al., 2016). The vertical resolution of the seismic lines presented in this study is between 30 cm and 10 m, depending on its

stratigraphic position and seismic source. On seismic reflection profiles, a sharp interruption of the lateral continuity of well-layered deposits with top and bottom unconformity surfaces corresponds to the typical seismic facies of MTDs. The facies usually displays low-amplitude chaotic reflectors (Loncke et al., 2009; Moscardelli and Wood, 2008). In sub-bottom parametric profiles, the MTDs upper and lower boundaries are high amplitude reflectors denoting a high impedance contrast with the surrounding well-layered deposits (Fig. 5). Basal discontinuities sometimes correspond with erosional surfaces. Submarine landslide deposits observed on the seismic reflection lines can result from successive events with amalgamated deposits (mass transport complex) or from a single event (MTD) (Moscardelli and Wood, 2008). Discriminate multistage processes with the vertical resolution of the available dataset appears difficult, thus we thereby named all the mapped landslide deposits MTDs, even if some of them seem to belong to mass transport complex features (Moscardelli and Wood, 2008).

The mapping procedure used follows most of the suggestions provided by the global approach of Clare et al. (2019). We selected eight parameters (descriptors) to compare landslide events (Fig. 5; Appendices A1 to A4):

- six quantitative morphometric parameters including deposit surface (km^2), current and decompacted deposit volumes (both in km^3), runout (km), scarp height (m), and scar slope (degrees)
- two qualitative parameters: the type of MTD (debris flow deposit or slide deposit) and the presence or absence of an erosive base.

Some differences in seismic facies allow classifying them into debris flow deposit or slide deposit (Appendices A1 and A2):

- Debris flow deposit: Internal structure generally lacks coherent reflectors and appears acoustically transparent, semi-transparent, sometimes chaotic.
- Slide deposit: Highly disorganized sediments, locally with hyperbolic diffractions and/or continuous bedding. The same landslide can display different types of facies depending on the seismic source.

Each mapped submarine landslide has an associated volume of reworked material representing the MTD (Figs. 5A and B). For some landslides, it has been possible to link this deposit (MTD) and its associated scar (Fig. 5). In such cases, the runout distances between scars and deposits were computed. Conversely, when scars were not recognized, the minimum runout was estimated as the landslide deposit's length, as Urgeles and Camerlenghi (2013) suggested. Parameters for all mapped landslides, west and east of the Al Idrissi fault zone, are provided in Appendix (Tables A1 and A2) and

illustrated in Figure 2B. Two deposits at equivalent stratigraphic positions are described independently and interpreted as different events, although they could correspond to a unique event. This limitation is not a major issue since the purpose of the article is to discuss the causal factors of landslides independently of their dynamics.

For each mapped MTDs, we used kriging interpolation to create isopach maps. In order to convert two-way travel time into metric units, P-wave velocities between 1550 m.s⁻¹ for superficial and near-surface MTDs mapped with parametric records and 1650 m.s⁻¹ for buried MTDs mapped with the Sparker and airgun sources have been used (Vp values from ODP sites are taken from Martinez-Garcia et al., 2013; see Appendix A3). From mapped MTD surfaces (Fig. 5), present-day volumes are estimated.

We determined decompacted MTD volume considering the following porosity law:

$$Porosity (\phi) = 73 - 9(\log_{10} d) \quad (1)$$

with depth (d) measured at ODP boreholes 976 and 979 (Eq. 1). The depth variation of porosity values for the upper 400 m of recovered materials on ODP sites 976 and 979 is given in Appendix A4. From the porosity law, the decompacted MTD volume (V₀) can be estimated using final porosity and volumes (ϕ_n and V_n, respectively) using Eq. 2:

$$V_0 = \frac{(1 - \phi_n)V_n}{(1 - \phi_0)} \quad (2)$$

3.4. Factor of safety approach for slope stability analysis

Causal factors of submarine landslides are usually discussed through the interaction between preconditioning factors and triggering mechanisms. Preconditioning factors are related to properties of the sediments acquired during or evolved from the primary depositional process and act in longer time-scales (e.g. > 0.1 ky). It can include for instance high pore (gas and water) pressure caused by rapid sedimentation or gas seepage, the presence of contrasting hydro-mechanical properties within sedimentary layers, or over-steepening of the slope gradient (Lee et al., 2007). This list is not exhaustive but illustrates most of the causal factors that deserve to be investigated in the Alboran Sea. At shorter timescales (e.g. seconds to decades), triggering mechanisms are considered initiating the slope failure by exerting external forces. They are as diverse as earthquakes, consequences of eustatic variations, tectonic movements or bottom currents eroding the toe of the slope (Rebesco et al., 2014). According to the local context, we evaluate the role of seismicity on the stability of a range of slopes by calculating the factor of safety (FOS). A slope is considered to be under stable conditions when the

resisting and driving forces are equal and under unstable conditions when the driving forces (stresses) exceed strengths. The FOS (Eq. 3) is defined as follows:

$$FOS = \frac{\text{resisting forces}}{\text{driving forces}} \quad (3)$$

The FOS can be calculated using a range of approaches, including the one-dimensional infinite slope method, the more sophisticated limit equilibrium analysis and the continuum mechanics methods in two and three-dimensions (Taylor, 1948). In the absence of required in situ data to perform improved slope stability analyses (i.e. in situ pore pressure conditions and mechanical properties of the sediments investigated), we choose the infinite slope and the pseudo-static approaches to evaluate in one dimension:

- the critical slope value based on the infinite slope approach (FOS_{is}) (Milledge et al., 2012)
- the role of earthquakes based on the pseudostatic approach (FOS_{ps}) (Kramer, 1996)

For a matter of simplification, the following assumptions are made:

- investigated contourites are fine-grained in agreement with stratigraphic analyses (Juan et al., 2020) and present a mean sediment unit weight of $18 \text{ kN}\cdot\text{m}^{-3}$, the cohesion may vary from 0 to 10 kPa and mean friction angle of 30° , although at failure the critical friction angle may be as low as 10° (Ouyang and Mayne, 2017).
- the sediment column investigated is not affected by pore water pressures in excess of hydrostatic ($u = u_h; \Delta u = 0 \text{ kPa}$)
with u the pore fluid pressure, u_h the hydrostatic pressure and Δu the excess pore pressure
- sliding occurs along a pre-defined plane parallel to the face of the slope (according to the infinite slope approach)
- the failure can be approached by the Mohr-Coulomb criteria (Rashid et al. 2017).

3.4.1. Infinite slope approach (FOS_{is})

This method postulates that a potential failure surface is parallel to the local topography and located at a depth (H) smaller than the length (L) of the slope (Taylor, 1948). The slope can thus be considered as being of infinite length and width so that stresses are the same on the two planes perpendicular to the slope. These stresses are collinear, equal in magnitude and opposite in direction; therefor they balance each other out and can be ignored. This assumption has been proved valid for landslides with $H/L < 0.06$ (Milledge et al., 2012). Most of the landslides investigated show $H/L < 0.075$ (Appendices A1 and A2). The expression of the FOS following the one-dimensional infinite slope approach (FOS_{is}) is:

$$FOS_{is} = \frac{\text{shear strength}}{\text{gravity forces}} = \frac{\tau_f}{\tau} = \frac{c' + \cos \beta \cos \beta z (\gamma_s - \gamma_w) \tan \phi'}{\gamma_{sat} \cdot z \cdot \sin \beta \cdot \cos \beta} = \frac{c'}{\gamma_{sat} \cdot z \cdot \sin \beta \cdot \cos \beta} + \frac{\tan \phi'}{\tan \beta} \quad (4)$$

Where c' is the effective soil cohesion (kPa), β is the slope inclination to the horizontal (rad), z is the depth of the sliding plane (m), ϕ' is the effective friction angle (rad), γ_{sat} the saturated sediment unit weight (kN/m³), γ_w and γ_s the water and sediment unit weight (kN/m³). Details about Eq. 4 are given in Appendix A5.

3.4.2. Pseudostatic approach (FOS_{ps})

Although submarine landslides may occur without any seismic triggering, global compilations of earthquake-induced landslides illustrate that MTD areas correlate reasonably well with earthquake-prone areas (Keefer, 1984; Rodriguez et al., 1999). According to Keefer (1984), the minimum earthquake magnitude that triggers landslides is generally $M_L = 5.5$ ($\sim M_W = 5.6$).

In our study, the influence of earthquakes has been attempted by using the pseudo-static FOS_{ps} approach (Kramer, 1996; Eq. 5). It represents the effects of the inertial forces F_h and F_v which act on the centroid of the failure mass during an earthquake (Appendix A5B). These two forces are dependent on pseudostatic seismic coefficients at the horizontal and vertical directions (k_h and k_v , respectively), which are linked to the recorded earthquake ground accelerations (Appendices A5 to A6). The selected expression of the pseudostatic approach, FOS_{ps} given in Eq. 6, is further detailed in Appendix (A5).

$$FOS_{ps} = \frac{\text{resisting forces}}{\text{static} + \text{pseudostatic driving forces}} \quad (5)$$

$$FOS_{ps} = \frac{c'_L + [(W - F_v) \cos \beta - F_h \sin \beta] \tan \phi}{(W - F_v) \sin \beta + F_h \cos \beta} \quad (6)$$

Where c'_L and ϕ are the Mohr-Coulomb strength parameters that describe the shear strength on the failure plane, W is the weight of the slope wedge involved in the failure and β the slope gradient. F_h and F_v are the inertial (pseudostatic) forces that act through the centroid of the failure mass. Values of k_h from 0 to 0.2 were selected to investigate the impact of earthquakes on the FOS_{ps} , with $k_h = 0.2$ corresponding to violent and destructive earthquakes (Kramer, 1996). As a matter of illustration, in the study area, the maximum moment magnitude recorded during monitored earthquake crisis in 2016 does not exceed 6.4 (Gracia et al. 2019), thus the potential seismicity in the study areas should not exceed $k_h > 0.2$. The ground acceleration depends on the seismic coefficient (Appendix A6) and varies according to the epicentral distance (Idriss, 1991). Epicentral distances are considered the distance between landslide scars and earthquake epicentres. The empirical correlation of Idriss (1991) relating earthquake magnitudes and the attenuation of the peak ground acceleration (PGA) with the

epicentral distance is used to confirm/discard whether the seismicity may trigger slope failures according to Eq. 5 and 6 (Appendix A6).

3.4.3. Estimation of moment magnitude M_w

Based on the equations from Yen and Ma (2011) and following the framework of Stirling et al., (2013) relating fault surfaces and earthquake magnitudes, the potential moment magnitudes that could be expected for compressive structures can be estimated.

Because the Alboran Sea is a slowly deforming area with deformation rates under 10mm/y (d'Acremont et al., 2020), we used the relationship of Yen and Ma (2011) for dip-slip earthquakes:

$$\log(\text{Surface}) = a \cdot \log(M_0) + b;$$

$$a = 0.8 ; b = -12.45$$

$$\log(M_0) = 1.5 \cdot M_w + 16.05$$

where M_0 is the seismic moment; M_w the moment magnitude; a is the intercept, b is the slope. See §4.5 for the calculation of fault surface.

4- Results

4.1- Distribution of the Mass Transport Deposits

A total of 67 submarine landslide features, including scars, deformation fronts, and deposits (Fig. 5) were described in the two SAR and SAB study areas (west and east of the AIFZ respectively, Figs 2B, 6 to 8; Appendices A1, A2). Twenty-eight MTDs have been determined in the SAR region (Appendix A1) and thirty-eight in the SAB region (Appendix A2). MTD scars are either located along steep ($>10^\circ$) to moderate ($5-9^\circ$) to gentle ($2-4^\circ$) slopes (Figs 3 and 8). Most of the MTDs are concentrated at the toe of the plastered drifts (Fig. 8) where slope gradients are moderate to steep (6 to 9° ; Fig. 3B) as occurred in the SAR region (Fig. 3B) or very low (2 to 5° ; Fig. 3C) as observed in the SAB region along the northern Pytheas bank.

The SAB is a NE-SW striking synform, eastward of the AIFZ, limited northward and southward by the Alboran Ridge and the Pytheas Bank, respectively (Fig. 3). In this area, MTDs are present in the SAB between 760 and 1100 m. MTD scars are present on the steep ($>10^\circ$) slope of the Alboran Ridge and the flatter ($2-4^\circ$) slope of the southward limb of SAB synform (Figs 2B, 3, 7). Scars found on the steep slopes of the Alboran Ridge coincide with a thrust-anticline structure (Fig. 3C). Sediment failures mobilize the plastered drifts from the northern flank of the Pytheas Bank, whereas the southern edge of the Alboran Ridge lacks well-expressed contourite drifts.

In the SAR, westward of the AIFZ, MTD scars are present along moderate slopes (6-9°) between 750 and 1125 m (Figs 6 and 8). Those scars seem to coincide with blind thrusts and edges of contourite plastered drifts (Figs. 3 and 8). The scars correspond to MTDs present in the deeper part of the basin between 1300 and 1400 m, where their clear bathymetric and stratigraphic signature are visible (Fig. 8). They exhibit a ≤ 10 m positive topography and transparent seismic facies (Figs 3, 6, and 7). Through the sedimentary sequence, historical landslide events are recognized at the foot of the SAR and AR structural highs in the deep basin (Figs 2C, 6, and 7).

Along the AIFZ, south of the Francesc Pagès seamount and north-west of the Alboran Ridge, no significant MTDs have been identified through the sedimentary record (Figs 2B and 8).

4.2. Volumes and relative ages of the MTDs

The decompacted volumes of the investigated MTDs (from 0.01 to ~ 15 km³; Fig. 9; Appendix A1, A2) are of comparable magnitude as submarine landslides in most of the Mediterranean Sea (Urgeles and Camerlenghi, 2013). In the SAR region, estimates of decompacted volumes of Pleistocene MTDs range between 0.01 and 10.5 km³ (Fig. 9; Appendix A1). In the SAB region, MTDs decompacted volumes from the southern flank of the Alboran Ridge range between 0.01 and 2.95 km³ (average value = 0.41 km³) and between 0.02 to ~ 15 km³ MTDs (average value = 4.8 km³) for MTDs from the northern slope of the Pytheas Bank (Fig. 9; Appendix A2).

MTDs observed on the bathymetric and seismic reflection data through the sedimentary sequence are younger than the Q1 (1.12 Ma) reflector (Figs 2B and 9). In the SAR region, the twenty-eight MTDs west of the AIFZ, are younger than 0.7 - 0.79 Ma (Q2 reflector to the seafloor; Fig. 9). In the SAB, the thirty-eight MTDs are younger than 1.12 Ma (Q1 reflector; Fig. 9). A Messinian buried MTD is identified (under the M reflector, Gorini et al., 2012) on the northern front of the SAR and in the south Alboran Basin (Figs 2B, 6 and 10). With a volume of 200 km³, an area of 550 km² and a maximum thickness of 540 m, this giant MTD extends for over 40 km from the Xauen/Tofino banks to the deep basin floor of the Western Alboran Basin (Gorini et al 2012).

4.3. Structural and fluid escape features

The SAR and Alboran Ridge are folded by a series of synclines and anticlines and bounded by blind E-W and NE-SW thrust faults, respectively (Figs 3B, C and 8). On the edges of these highs, the slope becomes steeper ($>10^\circ$) (Fig. 3). The north verging blind thrusts (DF1, DF2, DF3) affect the Messinian surface and the Pliocene-Quaternary contourite drift deposits are uplifted with a northern vergence (Figs 3B; 6 and 10). The sinistral AIFZ offsets the folded structural highs (Fig. 2A). MTDs described in

the previous section are not aligned along the NNE-SSW AIFZ but along these folded structural highs (Fig. 2B).

In the SAR region, fluid escape features, such as pockmarks and mud volcanoes, are clearly expressed on the seabed by circular depressions and mounds, respectively (Figs 1 inset; 8 and 10). All the mapped pockmarks constitute two main fields oriented ENE-WSW located on the northern and southern flank of the SAR into plastered drifts (Figs 8). On the southern flank of the SAR, the pockmarks are aligned following the DF2 blind thrust sub-parallel to the Xauen-Tofiño banks (Fig. 8). The pockmarks are imaged at the subsurface as vertical pipes with low seismic amplitudes, indicating the circulation of fluids (Fig. 10). Acoustic blanking zones extends from the messinian reflector (above a buried landslide) to the seabed as a set of columnar shapes (Fig. 10).

Almost all mapped pockmarks are concentrated west of the AIFZ, where thick contourite deposits are present (600 msec TWTT since Pliocene time; Figs 6, 7, 10). The spatial relationship between fluid escape features along normal faults, blind thrusts, as well as the existence of MTD scars on the steeper slopes of the plastered drifts, is illustrated in Figures 3B.

4.4. Slope stability analysis

Calculations of the factor of safety (FOS) based on the infinite slope (FOS_{IS}) illustrate that the contourites investigated are stable for slope gradients higher than the friction angle (ϕ), independently of the cohesion (Fig. 11). For the three landslide fields (LF), namely the Xauen LF, Central and Pytheas LF, we found that instability may be only attained if ϕ reduces substantially, down to 10° . These results illustrate that slope steepness has no negative effects if the frictional properties are high (30° , Fig. 11). However, when combining both low friction angle ($< 10^\circ$) and seismic activity ($0 < K_h < 0.2$), we found that the seafloor within the landslide fields (from scars to the deposits) may be affected by unstable configurations (Fig. 12).

To discuss the influence of earthquakes in triggering landslides, three landslide fields are defined according to their mean slope values and to their distance (from scars) to the main faults and/or to the epicentral earthquake locations (Figs 2 and 13):

- the Xauen landslide field where MTD scars are located along moderate to steep slope ($6-9^\circ$), where fluid escape features are present above blind thrust faults. MTD scars are at least 20 km west of the seismogenic AIFZ and less than 5 km from thrust faults DF1 and DF2, in the western part of the SAR region (Fig. 2A-B).
- The Central landslide field, where MTD scars are located along moderate to steep slope ($6-9^\circ$) is the closest to the AIFZ in the eastern part of the SAR region.

- The Pytheas landslide field, in the SAB region, where MTD scars are located along steep slopes ($>15^\circ$) on the Alboran ridge (i.e. thrust and fold, Fig.1) and on a gentle slope ($2-5^\circ$) on the northern Pytheas bank, both areas located more than 30 km from the AIFZ, Yusuf and Averroes faults.

For instance, $k_h > 0.1$ may destabilise the Pytheas LF whereas relatively low k_h values ($k_h \sim 0.05$) are enough to trigger landslides in the Central and Xauen LF (Fig. 12). Depending on the nature of the contourites, their friction angle (ϕ) may vary and be relatively low (10°) compared to mean values (30°) (Ouyang and Mayne, 2018), which facilitates slope failure. According to these values of ϕ , and the link between the horizontal seismic coefficient and the peak ground acceleration, the following hypotheses can be considered:

- for contourites with $\phi \sim 30^\circ$, the required seismic coefficient to trigger failure is $k_h > 0.1$, i.e. $\text{PGA} \geq 0.2 \text{ g}$. This PGA value is considered as the upper boundary required to destabilise sediments with classical frictional values.
- for contourites with $\phi \sim 10^\circ$, k_h values around 0.05 may trigger failure, which corresponds to $\text{PGA} = 0.1 \text{ g}$. Accordingly, this PGA is considered the lower bound required to destabilise sediments with reduced frictional values.

4.5. Seismic potential of faults

Based on the depth converted profiles published in d'Acremont et al., (2020), we have estimated the surfaces of the thrusts DF1 and DF2 beneath the MTD's scars and the scaled moment magnitude M_w during their reactivation (Table 1, Appendix A6). Our estimate of the ruptured surface supposes that, in the SAR, thrust faults are shallow and root in a deep weak layer of under-compacted shales (d'Acremont et al., 2020). DF1 and DF2 are then approximated to faults of 4 km deep, with 30° dip and 8 km length (Figs 7 and 8). Potential earthquakes have also been estimated in the Alboran Ridge according to the geometry of the reverse fault defined in Martinez-Garcia et al. (2013 and 2017) (Table 1). The Alboran Ridge main thrust fault (Fig. 8) is then approximated to a fault segment of 5 km in depth and 57 km in length. A similar dip than the DF1 and DF2 thrusts was used (30°). From these rough fault characteristics, we estimate scaled moment magnitudes ranging from $M_w = 6.1$ and 6.7 (Appendix A7). Considering that the entire surface of the mapped faults would break, the moment magnitude is overestimated, our values are therefore to be considered as an upper bound.

Faults	Length (Km)	Surface (km ²)	$M_{w_}(W)$	$M_{w_}(YaM)$
DF1a	18.71	149.69	6.50	6.49
DF2a	21.24	169.91	6.61	6.53

DF1b	16.74	133.92	6.41	6.45
DF2b	12.52	100.16	6.17	6.34
ARDF	57	285	6.17	6.72

Table 1: Scaled moment magnitudes (Mw) for compressive structures present on the Xauen landslide field (DF1 and DF2) and the major thrust of the Alboran Ridge deformation front (ARDF). Values are calculated according Wesnousky et al. (1983) (W) and Yen and Ma (2011) (YaM) approaches. See Appendix A7 for the location of the faults.

5- Discussion

The fact that high numbers of MTD events can occur along low gradient slopes indicates that gravity is not the main force leading the slope to fail in SAR and SAB regions as FOS values of ~ 1.1 for gradients $< 30^\circ$ suggests (Fig. 11). Therefore, other processes seem to be controlling sediment failure.

5.1. Influence of slope gradient, sedimentation, oceanographic fluctuation and fluid escape on the distribution of MTDs

5.1.1 Volume of MTD versus slope

In the SAB region, MTD volumes are higher when the source comes from the gently dipping ($2-5^\circ$) northern Pytheas bank (average of $\sim 4.8 \text{ km}^3$), compared to those who originate from the steep ($>10^\circ$) slope of the Alboran Ridge (average of 0.4 km^3 ; Figs. 3, 8, 9 and 10, Appendix A2). Since MIS 8, a significant frequency of low-volume MTDs are recorded in the sediment column, they originate from scars located on the steep Alboran Ridge slope (9 MTDs, Fig. 9). This demonstrates that the steeper the slope is, the higher the frequency of slope failures is, the lower the volume of each MTD event are (Fig. 9). Indeed, the slope gradient influences the failure frequency and sediment thickness involved in the failures. In high slope area, the rupture area is limited and continuous instability can favour more collapses at adjacent locations. The size of the surface available for sediment destabilization also depends on the slope values. The gentler the slope at the scars area, the greater is the volume potentially destabilized (e.g. Urlaub et al., 2015). On the high slope gradients of the Alboran Ridge, thin packages of contourite sediments are subject to sliding (Figs. 2B,3 and 9), as demonstrated by the decompacted volumes (average of 0.4 km^3) interpreted as evidences of a continuous destabilization on a steep slope. In the SAB, the relatively lower slope gradients ($2-5^\circ$) of the Pytheas Bank would explain less frequent (3 MTDs identified since MIS8 compared to 9 from the AR source) but more voluminous events, which can be as high as 15.6 km^3 (Fig. 9; Appendix A2).

482

483 5.1.2 Overpressure versus sedimentation rates and tectonics

484

485 High sedimentation rates in the mounded part of the investigated contourites could have generated
486 pore fluid pressures as described by Rebesco and Camerlenghi (2008) and potentially fluid escapes (i.e.
487 pockmarks; Figs 8 and 10). As a consequence, the reduction of the effective stress which has a negative
488 effect on the sediments strength, can certainly impact the slope stability (Laberg and Camerlenghi,
489 2008). Previous observations from the Mediterranean Sea show that fluid escape features lower the
490 sediment strength (Blinova et al., 2011; Pérez-Belzuz et al., 1997; Somoza et al.; 2012, Lafuerza et al.,
491 2012; Urgeles and Camerlenghi, 2013).

492 The sedimentation rates recorded from ODP sites 976 and 979 for the Quaternary period are 34 cm/ky
493 and 20 cm/ky respectively (Comas et al., 1996). Based on the available stratigraphic framework (Fig. 4;
494 Appendix A3), Pliocene-Quaternary estimated sedimentation rates for the contourite drifts range
495 between 7 and 32 cm/kyr. In the mounded part of Alboran Sea contourites, Alonso et al. (2021)
496 reported sedimentation rates of 11-190 cm/ky for the Late Pleistocene to Holocene periods. Although
497 variable, they include high sedimentation rates, which supports our hypothesis. Furthermore, if
498 contourites contain permeable lenses, lateral transfer of fluids could be expected downslope and
499 explain the concentration of submarine slide scars at the edge of contourite drifts north of the SAR
500 (Fig. 3B).

501 The SAR and SAB regions are very contrasting in terms of fluids and sedimentary escape features (mud
502 volcanoes and pockmarks). West of the AIFZ, seismic data reveal that pockmarks affect uplifted
503 contourite drifts (Figs 3B, 6, 8, and 10) and these pockmarks fields are inline above the DF2 blind thrust
504 fault (Figs 2 and 6). East of the AIFZ, no major fluid and sedimentary escape features are detected at
505 the bathymetry resolution.

506 The slide scars are located between DF1 and DF2 (Figs 2 and 8) suggesting a structural control of both
507 pockmarks and MTD scar location. Differential-compaction normal faults are located at the top of blind
508 thrust faults that remobilize an old Messinian MTD (Figs 6 and 10; Gorini et al., 2012). These faults
509 allow fluids to migrate vertically from deep successions (including the Messinian landslide, Fig. 10)
510 toward the seabed. Pockmarks may develop in response to the fluid pipe propagation in
511 unconsolidated sediments in the near surface (Figs 3B, 6 and 10B). Similar spatial distribution of fluid
512 escape features controlled by buried landslides has been illustrated, for instance, in the Niger
513 submarine delta (Riboulot et al., 2013).

514 The presence of pockmarks at the top of contouritic drifts could indicate important fluid circulations
515 (Figs 3B and 10) that would precondition the slope stability as suggested by Baraza and Ercilla (1996);

Rebesco et al. (2014); Miramontes et al. (2018). We interpret that the distribution of MTDs east and west of the AIFZ is mainly driven by the location of the structural highs (Fig. 2C).

5.1.3 Weak layer formation versus oceanographic fluctuations

Contourites are typically described in literature as sources of weak layers acting as a potential preconditioning factor of slope failure (Rebesco, 2005; Laberg and Camerlenghi, 2008; Rebesco et al. 2014). The type of deposit, the grain size, and the thickness of contourite drift vary with the sea-level fluctuations and changes in the bottom current intensity (Ercilla et al., 1994; Juan et al., 2016; Alonso et al., 2021) and drive the occurrence of weak layers.

Coarse-grained contourites (sand-sized) may undergo more easily liquefaction in response to cyclic loading, possibly inducing failure (e.g. Sultan et al., 2004). Cyclic loading could result from the high frequency and high amplitude glacio-eustatic fluctuations, which profoundly modify the slope stability since mid-Calabrian times (1.12 Ma) (Rohling et al., 2014, Baraza et al., 1990; Casas et al., 2011). In the north and west margin of the Alboran Basin, Ercilla et al. (2002), Juan et al. (2016), Alonso et al. (2021) observe successions of sandy mud deposits and silty clay intervals during sea-level lowstand and highstand, respectively. Sandy contourites, related to periods of high-intensity bottom currents, are interbedded within fine-grained contourites (Ercilla et al., 2002; Alonso et al., 2021; López-Gonzalez et al., 2019).

Near the continental Moroccan margin, sandy contourites (with high liquefaction potential) are identified along the Ceuta drift (Ercilla et al., 2002) (Fig. 1). In the SAB region, plastered drift seems to be fine-grained at least since the last 25 ka and coarse-grained in the moat (Alonso et al., 2021). The presence or absence of coarse grains depends on current intensity which is maximum in the moat part whose location likely varies according to eustatic oscillations (Frigola et al., 2007). Studies in the Gulf of Cadiz have shown that the classical model of contourite grain-size sequences, depending of the bottom current intensity, is much more complex than expected (Mulder et al. 2013). This strong variability in grain-size suggests that it is very difficult to emphasize if weak layers of coarse grains sediments are likely to occur in the studied area without core analysis. Based on these arguments we make the hypothesis that most of the contourite affected by the landslide scars (Fig. 8) are fine-grained but sand cannot be excluded if the moat was closer in the past.

5.2. Influence of growth folds and thrust faults on the distribution of the MTD

We propose that the SAR and Alboran Ridge tectonic structures control the distribution of the MTDs. MTDs are inline with the direction of blind thrusts and axial planes of folds (Fig. 2B). These tectonic

structures form topographic highs, interacting with the dense bottom current circulation, and favouring local contourite drift sedimentation.

Along the seismogenic AIFZ, MTDs are noticeably less abundant than further east and west (Figs 2 and 9). The available seismic reflection coverage south of the SAR highlights this paucity of submarine landslides (Fig. 2). This surprising observation can be related to “seismic strengthening” by earthquakes (Sawyer and DeVore 2015; Ten Brink et al., 2016). In the AIFZ repeated exposure to earthquake energy could gradually increase shear strength by shear-induced compaction (Sawyer and DeVore, 2015).

North of the SAR, the MTD scars (Figs 2B and 3B) are above the normal faults on top of the frontal DF1 blind thrust. The DF1 and DF2 blind thrusts uplift the northern wedge of the contourite drift (Figs 6 and 10B). The MTDs are distributed in the deep basin parallel to the headwall of the DF1 blind thrusts (Figs 2B and 8). Also, thrusting results in steeper slopes than folding, as observed North of the Xauen-Tofiño banks and along the Alboran Ridge (Fig. 3B, C). The northward and southward thrust vergences along the Xauen- Tofiño banks and Alboran ridge respectively, control the local slopes leading to the location of landslides.

Blind thrusts and folds are active since the late Tortonian, with a last tectonic phase starting around 1.8 Ma to 1.12 Ma illustrated by the DF1 to DF3 structures on the SAR (Martínez-García et al., 2013; Lafosse et al., 2020 and d’Acremont et al. 2020) (Fig. 2C). The creation of the topographic barriers generates an uneven seafloor on which contourite sedimentation began. However, observed MTD are younger than 1.12 Ma (Fig. 9). The vertical resolution of the seismic profiles (around 5 m) in deeper parts of the subsurface prevents the observation of MTDs thinner than 5 m. Increase of the MTDs volume after 1.12 Ma would only reflect this limitation in seismic resolution, rather than the absence of MTDs before 1.12 Ma. Despite this, the activity of these tectonic structures coincides roughly with the onset of MTD from 1.12 Ma. Tectonics creates topographic highs, beneficial for contourite drift growth (Juan et al., 2016) and slope failures.

5.3. What are the candidate faults triggering the submarine landslides?

To accommodate the oblique convergence between the African-Eurasian plates, strike-slip and reverse fault structures are present (Martínez-García et al., 2017; Estrada et al., 2018, 2021; d’Acremont et al. 2020; Lafosse et al. 2020). Based on the Idriss (1991) equation relating earthquake local magnitude M_l , epicentral distance and ground accelerations (Figs 12 and 13; Appendix A6), the minimum earthquake magnitude required to obtain the upper and lower bound of PGA, namely 0.1g and 0.2g in the investigated landslide fields are discussed below. Since PGA varies according to the distance (D) to faults, the earthquake magnitude is discussed considering the distance between the landslide field and the closest tectonic structure (Figs 12 and 13, Appendix A6):

- Pytheas LF is 40 km from Yusuf fault. At this site, PGA = 0.1 g can be obtained for a MI = 6.5 of both reverse and strike-slip style. Values of PGA = 0.2 g could occur only for MI = 8, which are too strong according to the recorded seismicity (Gracia et al., 2019). Therefore, these landslides could be explained as the result of the interaction between a moderate activity of the strike-slip Yusuf fault and a contourite characterised by reduced friction angle. Seismic reflection studies propose that the Averroes fault links with the Yusuf fault segment since 1.1 Ma (Perea et al., 2018; Martínez-García et al., 2013), suggesting generation of earthquakes up to Mw = 7.6 (Perea et al., 2018). Then, magnitudes high enough to trigger the destabilization at a regional scale and leading to an increase of the volume of the MTD could be possible. Seismic events have been recorded in the South Alboran Basin, close to the Pytheas scars (Fig. 2A). However, those events seem too distant with too small magnitudes to generate the required ground acceleration.
- Pytheas LF is located at a distance of 10-20 km from the Alboran Ridge. At this site, PGA = 0.1 g is obtained for a MI = 5 of reverse style and values of PGA = 0.2 g for MI = 6.5 for a reverse style. Obtained values of MI suggest that active potential reverse faults along the Alboran Ridge can be a better candidate to generate sufficient ground acceleration and induce slope destabilization. We estimate potential earthquakes between Mw = 6.1 and 6.7 from these structures (Table 1, Appendix A7). Recent characterization of the earthquakes occurring during the 2016 crisis near the Al-Idrissi fault (Stich et al., 2020) shows that reverse foreshock occurred at a depth of 12 km, indicating crustal-scale reverse faulting on similarly oriented faults in the SAR and Alboran Ridge regions.
- The Central LF is 10 km west from the Al-Idrissi fault. Here, PGA = 0.1 g is attained by a MI = 5.5 of strike slip style and PGA = 0.2 g by a MI = 6 of strike-slip style. These results demonstrate that landslides observed in this area may have been triggered by faults of at least $5.5 < MI < 6$. This agrees with the average Mw = 6.4 earthquake on NNE-SSW structural segments reported on the AIFZ (Gràcia et al., 2019; Stich et al., 2020).
- The Xauen LF is located 5 km from thrust faults DF1 et DF2. On the other hand, the Xauen LF is more than 20 km west of the seismogenic AIFZ, which implies that the highest PGA expected for a MI = 6.4 would be lower than 0.1 g (Fig. 13). At this site, reverse faults of MI = 4 could have generated PGA = 0.1 g and of MI = 5 to generate PGA = 0.2 g. Moreover, this value is in the range of $M_w \approx 6$ calculated for potential reverse faults triggered by the DF1, DF2 and Alboran ridge thrusts (Figs 2C and 3B). Therefore, thrust faults DF1 and DF2 are the best candidates to trigger slope instabilities in this landslide field.

Several faults accommodate the Quaternary deformation and trigger earthquakes near the study areas (Figs 1 and 2A). The active AIFZ concentrates the seismicity (Fig. 2) with $M_w=6.4$ earthquakes on NNE-SSW structural segments (Galindo-Zaldivar et al., 2018; Gracia et al., 2019). The strike-slip Averroes and the Yusuf faults are less seismically active than the AIFZ (Estrada et al., 2021) but have an important topographic expression on the seafloor (Estrada et al., 2018; 2021). Away from the AIFZ, no significant earthquake has been reported during the historical and instrumental period along the SAR and Alboran Ridge (Source IGN 2022; Fig. 2A) but the MTDs are in line with local blind reverse faults (Fig. 2B). Above the frontal blind reverse fault (DF1) and the Alboran Ridge thrust front (AR, Fig. 1) the seafloor is disturbed (Fig. 10B) showing recent activity. Some authors propose that the blind reverse faults are active during Pliocene-Quaternary times to accommodate the regional shortening (Martínez-García et al., 2013; Lafosse et al., 2020; d'Acremont et al., 2020). Consequently, we propose that the Pytheas, Central and Xauen landslides fields could have been triggered by the AIFZ, Averroes/Yusuf fault segments and blind thrust faults.

Moreover, MTD occurrence since $\sim Q_2-Q_1$ (1.12-0.79 Ma) (Fig. 9), is consistent with the Alboran Sea tectonic reorganization occurring (i) along the Averroes and Yusuf Faults since 1.1 Ma (Martinez-Garcia et al. 2013, 2017, Perea et al. 2018); (ii) along the AIFZ and in the Nekor Basin after 1.12-0.8 Ma (Fig. 8)(Galindo-Zaldivar et al., 2018; Giaconnia, et al., 2015; Lafosse et al., 2016 and 2020); (iii) along the SAR and Alboran Ridge blind thrusts with their reactivation since 1.8-1.1 Ma (Martínez-García et al., 2013; Lafosse et al., 2016, 2020; d'Acremont et al., 2020).

6- Conclusions

Morphological and seismic reflection data reveal at least sixty-seven submarine MTDs within the Quaternary deposits in the southern part of the Alboran Basin. The factors resulting in slope failure in the Alboran Sea are diverse, and usually a combination of several factors is needed. Despite the reported effect of seismicity on slope stability, the distribution of recorded low to moderate magnitude earthquakes along the AIFZ does not seem to match the investigated landslides' location. Instead, the slope failures west of the AIFZ likely resulted from a combination of uplift of topographic highs, contourite drift build-up and fluid flow. East of the AIFZ, slope failures are located along the SW-NE trend of the Alboran Ridge. The morphological analysis reveals that most of the submarine landslides with high volumes occur at low slopes ($2-5^\circ$) mostly on the Pytheas Bank slopes, where active faults are far. The observation of MTDs recorded only from 1.1 Ma is consistent with the formation of the AIFZ around that time, supporting seismic shaking as the main triggering mechanism. Alternatively,

potential high sedimentation rates during the Quaternary contourite deposition may have generated pore fluid overpressure and upward fluid migration, as supported by the presence of a pockmark field reducing the sediment resistance. Slope stability analysis shows that if the slope stability is locally preconditioned (reducing friction angles up to 10°), the required PGA to trigger a slope failure may reduce (from 0.2 g to 0.1 g), and such a PGA value could be generated by the local blind thrusts in the Xauen landslide field. The exact ages of these MTDs and the geotechnical properties are necessary to address the link between seismicity, sedimentation, oceanographic fluctuations, tectonism, and submarine landslide processes.

Acknowledgements

We thank the members of the SARAS and Marlboro cruises in 2011 and 2012. Reviews by Daniel Minisini, Davide Gamboa and Aggie Georgiopolou are gratefully acknowledged. This work was funded by the French program *Actions Marges, Défi Risques Naturels* CNRS-IRD (MITI-ALARM) and UPMC-Emergence (ALARM project), the ALBAMAR JCJC ANR-17-03CE-0004, the EUOFLEETS program (FP7/2007-2013; n°228344), project FICTS-2011-03-01. Seismic reflection data were processed using the Seismic UNIX SU and Geovecteur© software. The processed seismic data were interpreted using Kingdom IHS Suite© software. This work also benefited from the DAMAGE (AEI/FEDER CGL2016-80687-R) and FAUCES (Ref CTM2015-65461-C2-R; MINCIU/FEDER) Projects financed by "Ministerio de Economía y Competitividad y al Fondo Europeo de Desarrollo Regional" (FEDER). This work acknowledges the 'Severo Ochoa Centre of Excellence' accreditation of ICM-CSIC (CEX2019-000928-S).

Seismic reflection and bathymetric data collected during the MARLBORO and SARAS cruises are stored at SISMER repository (<https://doi.org/10.17600/11480100>, <https://doi.org/10.17600/12450090>, and <https://campagnes.flotteoceanographique.fr/campagnes/12000010>). Landslide parameters for MTDs mapped during this study are given in the appendix.

Figure caption

Figure 1: Bathymetric map of the Alboran Sea showing the structural features of the area. Shaded bathymetry from compilation of ISTEP and CSIC multibeam cruises with GEBCO 2014 database, topography from SRTM database. Focal mechanism in black: 1994 main shock (El Alami et al., 1998; Biggs et al., 2006). Focal mechanism in red: 2004 main shock (van der Woerd et al., 2014). Focal mechanism in green: 2016 main shock (Kariche et al., 2017; Medina and Cherkaoui, 2017). Focal mechanism in orange: Location and moment tensor solution obtained for the 1910 Adra Earthquake from Stich et al. (2003). AF, Averroes Fault; AIFZ, Al Idrissi Fault Zone; A.Is, Alboran Island; AR, Alboran

Ridge (Alboran ridge thrust front, ARTF); CSF, Carboneras Serrata Fault; EAB, East Alboran Basin; FP, Francesc Pagès Seamount; IB, Ibn-Batouta Bank; JF, Jebha Fault; NB, Nekor Basin; NF, Nekor Fault; PB, Pytheas Bank; SAB, South Alboran Basin; SAR, South Alboran Ridge; TB, Tofiño Bank; WAB, West Alboran Basin; XB, Xauen Bank; YF, Yusuf Fault. Orange dashed areas SAB and SAR correspond to the two key sites of this study (South Alboran Basin and South Alboran Ridge respectively). Offshore structural features from Estrada et al. (2017); d'Acremont et al. (2020). Inset: water currents between Mediterranean Sea and Atlantic Ocean and main features of the basement. The arrows representing water masses are from Ercilla et al. (2019); AW, Atlantic Water; LMW, Light Mediterranean intermediate Water; DMW, Dense Mediterranean Water. (For interpretation of the references to colour in this figure legend, the reader is referred to the web version of this article.)

Figure 2: (A) Bathymetric and seismic epicentral map. Epicentres of the earthquakes recorded between 1964 and 2020 (Spanish Instituto Geografico Nacional (IGN) database). Landslide field location used in the text and Figure 9 (Xauen, Central and Pytheas) is represented by the white line. (B) Structural map (from d'Acremont et al. 2020; Lafosse et al. 2020) with the distribution of the submarine landslides from this study. Xx and Mx correspond to the code names of the MTDs described in this paper (see Appendix). DF1, DF2, DF3, deformation front highlighted by blind thrusts from d'Acremont et al. 2020. ARDF, Alboran Ridge Deformation Front from Martinez-Garcia et al. 2017. A.Is, Alboran Island; FP, Francesc Pagès Seamount; RM, Ramon Margalef High. (C) Swath bathymetric and seismic reflection coverage of the study area, from CONTOURIBER (2010), Marlboro-1 (2011), Marlboro-2 (2012), SARAS (2012), MONTERA (2012), and INCRISIS (2016) projects and the Fishing General Secretary (Spanish Government) (HR: high resolution; VHR: very high resolution). Thick lines correspond to seismic reflection profiles shown in this paper with the figure number.

Figure 3: (A) Slope map of Southern Alboran Sea and slope failures. A.Is, Alboran Island; FP, Francesc Pagès Seamount; RM, Ramon Margalef High. (B)(C) Bathymetric profiles located in (A) with structural shape, slope values (from d'Acremont et al. 2020). VE, vertical exaggeration. DF1, DF2, DF3, deformation front highlighted by blind thrusts. MTD, Mass Transport Deposit.

Figure 4: Chronostratigraphic units and seismic horizons using ODP sites 976 (Units from Juan et al., 2016). Benthic $\delta^{18}O$ curve from Lisiecki and Raymo (2005). Composite seismic reflection profile used to follow the chronostratigraphic units from the ODP site 976 to the study area. IB, Ibn Batouta; FP, Francesc Pagès, Mioc., Miocene; Mess., Messinian; H, Holocene; U upper. MIS 12 and MIS 8 represent Marine Isotope stages, we have used this term as the name of the reflectors.

Figure 5: Characterization of a submarine landslide using bathymetry (A), slope profiles (B, C, D) and seismic reflection profile (E): example of MTD X5 along the Xauen Bank northern flank. The white arrow indicates direction of transport of the submarine landslide.

Figure 6: High-resolution profile from Marlboro 1 campaign (MAR02), between the Xauen Bank (XB) and the southern WAB. It shows localization of landslide scars along slopes north to the Xauen Bank, where slope gradient is affected by contouritic sedimentation (Ceuta contourite drift) and northward vergence thrusts (DF1, DF2) as well as mass transport deposits (Xx mapped in Figure 2B). TB Tofiño Bank, FP Francesc Pagès Seamount, IB Ibn Batouta seamount. P0, P1, BQD, Q0, Q1, Q2, MIS12 and MIS8 refer to seismic reflectors defined in figure 4.

Figure 7: High-resolution profile from MONTERA campaign (AL04), in the southern SAB. It highlights buried MTDs downward the slope and three decollement levels above the Q1 reflector. Mx Mass transport deposits represented in map Figure 2B. AR Alboran Ridge, PB Pytheas Bank, M, P0, P1, BQD, Q0, xx refer to seismic reflectors defined in figure 4.

Figure 8: Morpho-structural map of the study area. Contourite deposits from Ercilla et al. 2019, structural features from d'Acremont et al. (2020) and Lafosse et al. (2020). A.Is, Alboran Island; BBFZ, Boussekkour-Bokkoya Fault Zone; FP, Francesc Pagès Seamount; RM, Ramon Margalef High. DF1, DF2, DF3, deformation front highlighted by blind thrusts.

Figure 9: Distribution of MTDs observed and quantified in the southern part of the Alboran Sea, west and east of the AIFZ. The three landslide fields are localized in the Figure 2A: Xauen landslides field north to the Xauen and Tofiño Banks; Central landslides field north of the Francesc Pagès Seamount; Pytheas landslides field between the Alboran Ridge and the Pytheas bank. The MTDs are represented according to their age, volumes and for those in the east, their sources. See Appendices A1 and A2 for MTD characteristics. Xx and Mx correspond to the code names of the MTDs described and shown in Figure 2B.

Figure 10: Fluid escape and compactional fault features through contourite drift in the SAR region (north Xauen Bank). A. Sub-seabed expression of fluid escapes and pockmarks on ultra-high resolution seismic reflection data (TOPAS). Location in B. B. High-resolution seismic reflection data showing the deformation below the contourite drift, associated to faults and fluid escapes. The normal faults here are interpreted as due to fold extrados extension from blind thrusts. Inset: in red location of MAR04 and TOPAS profiles, black rectangle corresponds to bathymetric zoom C. C. Seabed expression of

pockmarks and landslide scar. Bathymetric data with contours every 50m. XB, Xauen Bank; TB, Tofino Bank; RM, Ramon Margalef Seamount. (For interpretation of the references to colour in this figure legend, the reader is referred to the web version of this article.)

Figure 11: Factor of safety calculations based on the infinite slope approach (FOSIS) illustrating that according to the Mohr-Coulomb criteria, the minimum slope angle required to trigger a failure is the friction angle. Calculations for three values of cohesions illustrates the restricted effects on the stability. Area of the three landslide fields (LF) according to their slope gradients are represented in pink. ϕ friction angle (phi); Cohesion (XKPa). (For interpretation of the references to colour in this figure legend, the reader is referred to the web version of this article.)

Figure 12: Factor of safety calculations based on the pseudostatic approach (FOSPS) for seismic coefficients k_h from 0 to 0.2. Top: scenario of sediments with a friction angle of 30° . Bottom: scenario of sediments with a friction angle of 10° . Instability may be attained for the Xauen and Central Landslide Fields (LF) if $k_h > 0.05$, and for the Pytheas LF $k_h > 0.1$. ϕ friction angle; k_h pseudostatic seismic coefficient.

Figure 13: Peak Ground Accelerations (PGA) obtained for reverse and strike-slip earthquakes as function of the epicentral distance. k_h pseudostatic seismic coefficient. M_I earthquake magnitude. D -distance between the landslide field (scar features) and the closest tectonic structure (See Appendix A6 for details on the attenuation relationship).

References

- Alasset, P.-J., Hébert, H., Maouche, S., Calbini, V., Meghraoui, M., 2006. The tsunami induced by the 2003 Zemmouri earthquake (MW= 6.9, Algeria): modelling and results. *Geophys. J. Int.* 166, 213–226. <https://doi.org/10.1111/j.1365-246X.2006.02912.x>
- Alonso, B., Ercilla, G., García, M., Vázquez, J., Juan, C., Casas, D., Estrada, F., d'Acremont, E., Gorini, C., El Moumni, B., Farran, M., 2014. Quaternary Mass-Transport Deposits on the North-Eastern Alboran Seamounts (SW Mediterranean Sea), in: *Submarine Mass Movements and Their Consequences*. Springer, pp. 561–570.
- Alonso, B., Juan, C., Ercilla, G., Cacho, I., López-González, N., Rodríguez-Tovar, F.J., Dorador, J., Francés, G., Casas, D., Vadorpe, T., Vázquez, J.T., 2021. Paleooceanographic and paleoclimatic variability in the Western Mediterranean during the last 25 cal. kyr BP. New insights from contourite drifts. *Mar. Geol.* 106488. <https://doi.org/10.1016/j.margeo.2021.106488>
- Baraza, J., Ercilla, G., 1996. Gas-charged sediments and large pockmark-like features on the Gulf of Cadiz slope (SW Spain). *Mar. Pet. Geol.* 13, 253–261. [https://doi.org/10.1016/0264-8172\(95\)00058-5](https://doi.org/10.1016/0264-8172(95)00058-5)

- Baraza, J., Ercilla, G., Lee, H.J., 1992. Geotechnical properties and preliminary assessment of sediment stability on the continental slope of the northwestern Alboran Sea. *Geo-Mar. Lett.* 12, 150–156. <https://doi.org/10.1007/BF02084926>
- Baraza, J., Lee, H.J., Kayen, R.E., Hampton, M.A., 1990. Geotechnical characteristics and slope stability on the Ebro margin, western Mediterranean. *Mar. Geol.* 95, 379–393. [https://doi.org/10.1016/0025-3227\(90\)90125-4](https://doi.org/10.1016/0025-3227(90)90125-4)
- Blinova, V.N., Comas, M.C., Ivanov, M.K., Poludetkina, E.N., Matveeva, T.V., 2011. Active mud volcanism in the West Alboran Basin: Geochemical evidence of hydrocarbon seepage. *Mar. Pet. Geol.* 28, 1483–1504. <https://doi.org/10.1016/j.marpetgeo.2011.06.001>
- Calvert, A., Sandvol, E., Seber, D., Barazangi, M., Roecker, S., Mourabit, T., Vidal, F., Alguaeil, G., Jabour, N., 2000. Geodynamic evolution of the lithosphere and upper mantle beneath the Alboran region of the western Mediterranean: Constraints from travel time tomography. *J. Geophys. Res.* 105, 10871–10898.
- Calvès, G., Huuse, M., Clift, P.D., Brusset, S., 2015. Giant fossil mass wasting off the coast of West India: The Nataraja submarine slide. *Earth and Planet. Sci. Lett.* 432, 265–272. <https://doi.org/10.1016/j.epsl.2015.10.022>
- Carter, L., Gavey, R., Talling, P.J., Liu, J.T., 2014. Insights into Submarine Geohazards from Breaks in Subsea Telecommunication Cables. *Oceanography* 27, 58–67.
- Casas, D., Ercilla, G., Yenes, M., Estrada, F., Alonso, B., García, M., Somoza, L., 2011. The Baraza Slide: model and dynamics. *Mar. Geophys. Res.* 32, 245–256. <https://doi.org/10.1007/s11001-011-9132-2>
- Cattaneo, A., Babonneau, N., Ratzov, G., Yelles, K., Brac, R., 2012. Searching for the seafloor signature of the 21 May 2003 Boumerdes earthquake offshore central Algeria. *Nat. Hazards Earth Syst. Sci.* 2159–2172. <https://doi.org/10.5194/nhess-12-2159-2012>
- Chiocci, F.L., Romagnoli, C., Tommasi, P., Bosman, A., 2008. The Stromboli 2002 tsunamigenic submarine slide: Characteristics and possible failure mechanisms. *Journal of Geophysical Research* 113, 1–11. <https://doi.org/10.1029/2007JB005172>
- Clare, M.A., Clarke, J.E.H., Talling, P.J., Cartigny, M.J.B., Pratomo, D.G., 2016. Preconditioning and triggering of offshore slope failures and turbidity currents revealed by most detailed monitoring yet at a fjord-head delta. *Earth Planet. Sci. Lett.* 450, 208–220. <https://doi.org/10.1016/j.epsl.2016.06.021>
- Clare, M., Chaytor, J., Dabson, O., Gamboa, D., Georgiopoulou, A., Eady, H., Hunt, J., Jackson, C., Katz, O., Krastel, S., León, R., Micallef, A., Moernaut, J., Moriconi, R., Moscardelli, L., Mueller, C., Normandeau, A., Patacci, M., Steventon, M., Urlaub, M., Völker, D., Wood, L., Jobe, Z., 2019. A consistent global approach for the morphometric characterization of subaqueous landslides. *Geol. Soc. Lond., Spec. Publ.* 477, 455–477. <https://doi.org/10.1144/SP477.15>
- Colantoni, P., Gennesseaux, P.M., Vanney, J.R., Ulzega, A., Melegari, G., Trombetta, A., 1992. Processi dinamici del canyon sottomarino di Gioia Tauro (Mare Tirreno). *Giornale di Geologia. Giornale di geologica* 199–213.
- Comas, M., Platt, J.P., Soto, J.I., Watts, A.B., 1999. The origin and tectonic history of the Alboran basin: insights from leg 161 results. *Ocean Drilling Program* 161, 555–580.
- Comas, M.C., Zahn, R., Klaus, A., 1996. *Proc. ODP, Init. Reports.*
- d’Acremont, E., Gutscher, M.-A., Rabaute, A., de Lépinay, B.M., Lafosse, M., Poort, J., Ammar, A., Tahayt, A., Le Roy, P., Smit, J., 2014. High-resolution imagery of active faulting offshore Al Hoceima, Northern Morocco. *Tectonophysics* 632, 160–166.
- d’Acremont, E., Lafosse, M., Rabaute, A., Teurquety, G., Couto, D.D., Ercilla, G., Juan, C., Lépinay, B.M. de, Lafuerza, S., Galindo-Zaldivar, J., Estrada, F., Vazquez, J.T., Leroy, S., Poort, J., Ammar, A., Gorini, C., 2020. Polyphase tectonic evolution of fore-arc basin

- related to STEP fault as revealed by seismic reflection data from the Alboran Sea (W-Mediterranean). *Tectonics* n/a, e2019TC005885. <https://doi.org/10.1029/2019TC005885>
- Dan, G., Sultan, N., Savoye, B., 2007. The 1979 Nice harbour catastrophe revisited: Trigger mechanism inferred from geotechnical measurements and numerical modelling. *Mar. Geol.* 245, 40–64. <https://doi.org/10.1016/j.margeo.2007.06.011>
- Do Couto, D., Gorini, C., Jolivet, L., Lebre, N., Augier, R., Gumiaux, C., d'Acremont, E., Ammar, A., Jabour, H., Auxietre, J.-L., 2016. Tectonic and stratigraphic evolution of the Western Alboran Sea Basin in the last 25 Myrs. *Tectonophysics* doi:10.1016/j.tecto.2016.03.020. <https://doi.org/10.1016/j.tecto.2016.03.020>
- Dussauge, C., Grasso, J.-R., Helmstetter, A., 2003. Statistical analysis of rockfall volume distributions: Implications for rockfall dynamics. *Journal of Geophysical Research: Solid Earth* 108. <https://doi.org/10.1029/2001JB000650>
- Ercilla, G., Alonso, B., Baraza, J., 1994. Post-Calabrian sequence stratigraphy of the northwestern Alboran Sea (southwestern Mediterranean). *Marine Geology* 120, 249–265. [https://doi.org/10.1016/0025-3227\(94\)90061-2](https://doi.org/10.1016/0025-3227(94)90061-2)
- Ercilla, G., Baraza, J., Alonso, B., Estrada, F., Casas, D., Farrán, M., 2002. The Ceuta Drift, Alboran Sea, southwestern Mediterranean. *Geological Society, London, Memoirs* 22, 155–170. <https://doi.org/10.1144/gsl.mem.2002.022.01.12>
- Ercilla, G., Juan, C., Alonso, B., Estrada, F., Vázquez, J.T., Casas, D., Hernández-Molina, F.J., El Moumni, B., D'Acremont, E., Gorini, C., 2015. Interaction between alongslope and downslope sedimentary processes in the Alboran Sea during the Pliocene and Quaternary.
- Ercilla, G., Juan, C., Hernandez-Molina, F.J., Bruno, M., Estrada, F., Alonso, B., Casas, D., Ií Farran, M., Llave, E., Garcia, M., 2016. Significance of bottom currents in deep-sea morphodynamics: an example from the Alboran Sea. *Mar. Geol.* 378, 157–170.
- Ercilla, G., Juan, C., Periañez, R., Alonso, B., Abril, J.M., Estrada, F., Casas, D., Vázquez, J.T., d'Acremont, E., Gorini, C., El Moumni, B., Do Couto, D., Valencia, J., 2019. Influence of alongslope processes on modern turbidite systems and canyons in the Alboran Sea (southwestern Mediterranean). *Deep Sea Research Part I: Oceanographic Research Papers* 144, 1–16. <https://doi.org/10.1016/j.dsr.2018.12.002>
- Ercilla, G., Vázquez, J.-T., Alonso, B., Bárcenas, P., Casas, D., d'Acremont, E., Estrada, F., Fernández-Salas, L.M., Galindo-Zaldívar, J., Juan, C., Lobo, F., López-González, N., Palomino, D., Sánchez-Guillamón, O., Chourak, M., Gil, A., Gómez-Ballesteros, M., El Moumni, B., Peláez, J.A., Valencia, J., Gorini, C., 2021. Seafloor Morphology and Processes in the Alboran Sea, in: Báez, J.C., Vázquez, J.-T., Camiñas, J.A., Malouli Idrissi, M. (Eds.), *Alboran Sea - Ecosystems and Marine Resources*. Springer International Publishing, Cham, pp. 157–205. https://doi.org/10.1007/978-3-030-65516-7_6
- Estrada, F., Ercilla, G., Alonso, B., 1997. Pliocene-Quaternary tectonic-sedimentary evolution of the NE Alboran Sea (SW Mediterranean Sea). *Tectonophysics, Structural Controls on Sedimentary Basin Formation* 282, 423–442. [https://doi.org/10.1016/S0040-1951\(97\)00227-8](https://doi.org/10.1016/S0040-1951(97)00227-8)
- Estrada, F., Galindo-Zaldívar, J., Vázquez, J.T., Ercilla, G., D'Acremont, E., Alonso, B., Gorini, C., 2018. Tectonic indentation in the central Alboran Sea (westernmost Mediterranean). *Terra Nova* 30, 24–33.
- Estrada, F., González-Vida, J.M., Peláez, J.A., Galindo-Zaldívar, J., Ortega, S., Macías, J., Vázquez, J.T., Ercilla, G., 2021. Tsunami generation potential of a strike-slip fault tip in the westernmost Mediterranean. *Sci Rep* 11, 16253. <https://doi.org/10.1038/s41598-021-95729-6>

- Frigola, J., Moreno, a., Cacho, I., Canals, M., Sierro, F. J., Flores, J. a., Grimalt, J. O., Hodell, D. a., & Curtis, J. H., 2007. Holocene climate variability in the western Mediterranean region from a deepwater sediment record. *Paleoceanography* 22, 2.
<https://doi.org/10.1029/2006PA001307>
- Galindo-Zaldivar, J., Ercilla, G., Estrada, F., Catalán, M., d'Acremont, E., Azzouz, O., Casas, D., Chourak, M., Vazquez, J.T., Chalouan, A., 2018. Imaging the growth of recent faults: the case of 2016–2017 seismic sequence sea bottom deformation in the Alboran Sea (Western Mediterranean). *Tectonics* 37, 2513–2530.
- Giaconia, F., Booth-Rea, G., Ranero, C.R., Gràcia, E., Bartolome, R., Calahorrano, A., Iacono, C.L., Vendrell, M.G., Cameselle, A.L., Costa, S., Peña, L.G. de la, Martínez-Loriente, S., Perea, H., Viñas, M., 2015. Compressional tectonic inversion of the Algero-Balearic basin: Latemost Miocene to present oblique convergence at the Palomares margin (Western Mediterranean). *Tectonics* 34, 1516–1543.
<https://doi.org/10.1002/2015TC003861>
- Gorini, C., d'Acremont, E., El Abbassi, M., Do Couto, D., Migeon, S., Ammar, A., Estrada, F., Ercilla, G., Alonso, B., Poort, J., Jabour, H., 2012. Giant slide in the South Alboran margin: Upper Miocene margin inversion or Messinian sea level fall ? Presented at the EGU, Vienna (Austria).
- Gracia, E., Grevenmeyer, I., Bartolome, R., Perea, H., Martinez-Loriente, S., de la Peña, L.G., Villasenor, A., Klinger, Y., Iacono, C.L., Diez, S., 2019. Earthquake crisis unveils the growth of an incipient continental fault system. *Nature communications* 10, 1–12.
- Grevenmeyer, I., Gràcia, E., Villaseñor, A., Leuchters, W., Watts, A.B., 2015. Seismicity and active tectonics in the Alboran Sea, Western Mediterranean: Constraints from an offshore-onshore seismological network and swath bathymetry data. *Journal of Geophysical Research : Solid Earth* 120, 8348–8365.
<https://doi.org/10.1002/2015JB012073>.Received
- Gutscher, M.-A., Malod, J., Rehault, J.-P., Contrucci, I., Klingelhoefer, F., Mendes-Victor, L., Spakman, W., 2002. Evidence for active subduction beneath Gibraltar. *Geology* 30, 1071–1074. [https://doi.org/10.1130/0091-7613\(2002\)030<1071:EFASBG>2.0.CO;2](https://doi.org/10.1130/0091-7613(2002)030<1071:EFASBG>2.0.CO;2)
- Haflidason, H., Sejrup, H.P., Nygård, A., Mienert, J., Bryn, P., Lien, R., Forsberg, C.F., Berg, K., Masson, D., 2004. The Storegga Slide: architecture, geometry and slide development. *Marine Geology, COSTA - Continental Slope Stability* 213, 201–234.
<https://doi.org/10.1016/j.margeo.2004.10.007>
- Hampton, M.A., Lee, H.J., Locat, J., 1996. Submarine landslides. *Reviews of Geophysics* 34, 33–59. <https://doi.org/10.1029/95RG03287>
- Idriss, I.M., 1991. Earthquake Ground Motions at Soft Soil Sites. Presented at the Second International Conferences on Recent Advances in Geotechnical Earthquake Engineering and Soil Dynamics, St Louis, Missouri, p. 9.
- Jolivet, L., Augier, R., Faccenna, C., Negro, F., Rimmele, G., Agard, P., Robin, C., Rossetti, F., Crespo-Blanc, A., 2008. Subduction, convergence and the mode of backarc extension in the Mediterranean region. *Bull. Soc. géol. Fr* 179, 525–550.
- Jolivet, L., Faccenna, C., Piromallo, C., 2009. From mantle to crust: Stretching the Mediterranean. *Earth and Planetary Science Letters* 285, 198–209.
- Juan, C., Ercilla, G., Estrada, F., Alonso, B., Casas, D., Vázquez, J.T., d'Acremont, E., Medialdea, T., Hernández-Molina, F.J., Gorini, C., 2020. Multiple factors controlling the deep marine sedimentation of the Alboran Sea (SW Mediterranean) after the Zanclean Atlantic Mega-flood. *Marine Geology* 106138.
- Juan, C., Ercilla, G., Hernández-Molina, F.J., Estrada, F., Alonso, B., Casas, D., García, M., Llave, E., Palomino, D., Vázquez, J.-T., 2016. Seismic evidence of current-controlled

sedimentation in the Alboran Sea during the Pliocene and Quaternary:
Palaeoceanographic implications. *Marine Geology*.

Kariche, J., Meghraoui, M., Timoulali, Y., Cetin, E., Toussaint, R., 2018. The Al Hoceima earthquake sequence of 1994, 2004 and 2016: Stress transfer and poroelasticity in the Rif and Alboran Sea region. *Geophys J Int* 212, 42–53. <https://doi.org/10.1093/gji/ggx385>

Keefer, D.K., 1984. Landslides caused by earthquakes. *GSA Bulletin* 95, 406–421. [https://doi.org/10.1130/0016-7606\(1984\)95<406:LCBE>2.0.CO;2](https://doi.org/10.1130/0016-7606(1984)95<406:LCBE>2.0.CO;2)

Kramer, S.L., 1996. *Geotechnical earthquake engineering*. Prentice-Hall Civil Engineering and Engineering Mechanics Series.

Laberg, J.S., Camerlenghi, A., 2008. Chapter 25 The Significance of Contourites for Submarine Slope Stability, in: Rebesco, M., Camerlenghi, A. (Eds.), *Developments in Sedimentology, Contourites*. Elsevier, pp. 537–556. [https://doi.org/10.1016/S0070-4571\(08\)10025-5](https://doi.org/10.1016/S0070-4571(08)10025-5)

Lafosse, M., Acremont, E., Rabaute, A., L, B.M.D., Tahayt, A., Ammar, A., Gorini, C., 2016. Evidence of quaternary transtensional tectonics in the Nekor basin (NE Morocco). *Basin Research* 1–20. <https://doi.org/10.1111/bre.12185>

Lafosse, M., d'Acremont, E., Rabaute, A., Estrada, F., Jollivet-Castelot, M., Vazquez, J.T., Galindo-Zaldivar, J., Ercilla, G., Alonso, B., Smit, J., Ammar, A., Gorini, C., 2020. Plio-Quaternary tectonic evolution of the southern margin of the Alboran Basin (Western Mediterranean). *Solid Earth* 11, 741–765. <https://doi.org/10.5194/se-11-741-2020>

Lafuerza, S., Sultan, N., Canals, M., Lastras, G., Cattaneo, A., Frigola, J., Costa, S., Berndt, C., 2012. Failure mechanisms of Ana slide from geotechnical evidence, Eivissa channel, Western Mediterranean Sea. *Marine Geology* 307, 1–21.

Lee, H.J., Locat, J., Desgagnes, P., Parsons, J.D., McAdoo, B.G., Orange, D.L., Puig, P., Wong, F.L., Dartnell, P., Boulanger, E., 2007. Submarine mass movements on continental margins, in: *Continental Margin Sedimentation: From Sediment Transport to Sequence Stratigraphy*. p. 62.

Locat, J., Lee, H.J., 2002. Submarine landslides: advances and challenges. *Canadian Geotechnical Journal* 39, 193–212. <https://doi.org/10.1139/t01-089>

Loncke, L., Gaullier, V., Droz, L., Ducassou, E., Migeon, S., Mascle, J., 2009. Multi-scale slope instabilities along the Nile deep-sea fan, Egyptian margin: A general overview. *Marine and Petroleum Geology* 26, 633–646. <https://doi.org/10.1016/j.marpetgeo.2008.03.010>

López-González, N., Alonso, B., Juan, C., Ercilla, G., Bozzano, G., Cacho, I., Casas, D., Palomino, D., Vázquez, J.-T., Estrada, F., Bárcenas, P., d'Acremont, E., Gorini, C., Moumni, B.E., 2019. 133,000 Years of Sedimentary Record in a Contourite Drift in the Western Alboran Sea: Sediment Sources and Paleocurrent Reconstruction. *Geosciences* 9, 345. <https://doi.org/10.3390/geosciences9080345>

Macías, J., Vázquez, J.T., Fernández-Salas, L.M., González-Vida, J.M., Bárcenas, P., Castro, M.J., Díaz-del-Río, V., Alonso, B., 2015. The Al-Borani submarine landslide and associated tsunamis. A modelling approach. *Marine Geology*. <https://doi.org/10.1016/j.margeo.2014.12.006>

Marle, G., 2007. Subsea Landslide is Likely Cause of SE Asian Communications Failure., ICPC Press Release explaining the likely cause of submarine telecommunications failures following the subsea earthquake off Taiwan in 2006.

Martinez Garcia, P., Comas, M., Lonergan, L., Watts, A.B., 2017. From Extension to Shortening: Tectonic Inversion Distributed in Time and Space in the Alboran Sea, Western Mediterranean. *Tectonics* 36, 2777–2805. <https://doi.org/10.1002/2017TC004489>

- Martinez-Garcia, P., Comas, M., Soto, J.I., Lonergan, L., Watts, A.B., 2013. Strike-slip tectonics and basin inversion in the Western Mediterranean : the Post-Messinian evolution of the Alboran Sea. *Basin Research* 25, 361–387.
<https://doi.org/10.1111/bre.12005>
- Mauffret, A., Ammar, A., Gorini, C., Jabour, H., 2007. The Alboran Sea (Western Mediterranean) revisited with a view from the Moroccan Margin. *Terra Nova* 19, 195–203. <https://doi.org/10.1111/j.1365-3121.2007.00734.x>
- Mauffret, A., Maldonado, A., Campillo, A.C., 1992. Tectonic framework of the eastern Alboran and western Algerian Basins, western Mediterranean. *Geo-Marine Letters* 12, 104–110. <https://doi.org/10.1007/bf02084919>
- McAdoo, B.G., Pratson, L.F., Orange, D.L., 2000. Submarine landslide geomorphology, US continental slope. *Marine Geology* 169, 103–136. [https://doi.org/10.1016/S0025-3227\(00\)00050-5](https://doi.org/10.1016/S0025-3227(00)00050-5)
- Medina, F., Cherkaoui, T.-E., 2017. The South-Western Alboran Earthquake Sequence of January-March 2016 and Its Associated Coulomb Stress Changes. *OJER* 06, 35–54.
<https://doi.org/10.4236/ojer.2017.61002>
- Milledge, D.G., Griffiths, D.V., Lane, S.N., Warburton, J., 2012. Limits on the validity of infinite length assumptions for modelling shallow landslides. *Earth Surface Processes and Landforms* 37, 1158–1166. <https://doi.org/10.1002/esp.3235>
- Miramontes, E., Garziglia, S., Sultan, N., Jouet, G., & Cattaneo, A. (2018). Morphological control of slope instability in contourites: a geotechnical approach. *Landslides*, 15(6), 1085–1095. <https://doi.org/10.1007/s10346-018-0956-6>
- Moscardelli, L., Wood, L., 2008. New classification system for mass transport complexes in offshore Trinidad. *Basin Research* 20, 73–98. <https://doi.org/10.1111/j.1365-2117.2007.00340.x>
- Mulder, T., Hassan, R., Ducassou, E., Zaragosi, S., Gonthier, E., Hanquiez, V., Marchès, E., Toucanne, S., 2013. Contourites in the Gulf of Cadiz: a cautionary note on potentially ambiguous indicators of bottom current velocity. *Geo-Mar Lett* 33, 357–367.
<https://doi.org/10.1007/s00367-013-0332-4>
- Nadal, N., Amine, M.M., El Madani, K., 2018. Aquaculture marine marocaine : Potentiel et nécessités de développement (DEPF Etudes). Agence Nationale pour le développement de l'Aquaculture.
- Okal, E.A., Synolakis, C.E., Uslu, B., Kalligeris, N., Voukouvalas, E., 2009. The 1956 earthquake and tsunami in Amorgos, Greece. *Geophys J Int* 178, 1533–1554.
<https://doi.org/10.1111/j.1365-246X.2009.04237.x>
- Ouyang, Z., Mayne, P.W., 2017. Effective friction angle of soft to firm clays from flat dilatometer. *Proceedings of the Institution of Civil Engineers - Geotechnical Engineering* 170, 137–147. <https://doi.org/10.1680/jgeen.16.00073>
- Palano, M., González, P.J., Fernández, J., 2015. The Diffuse Plate boundary of Nubia and Iberia in the Western Mediterranean: Crustal deformation evidence for viscous coupling and fragmented lithosphere. *Earth and Planetary Science Letters* 430, 439–447.
<https://doi.org/10.1016/j.epsl.2015.08.040>
- Pelaez, J.A., Chourak, M., Tadili, B.A., Brahim, L.A., Hamdache, M., Casado, C.L., Solares, J.M.M., 2007. A Catalog of Main Moroccan Earthquakes from 1045 to 2005. *Seismological Research Letters* 78, 614–621. <https://doi.org/10.1785/gssrl.78.6.614>
- Perea, H., Gràcia, E., Martínez-Lorient, S., Bartolome, R., de la Peña, L.G., de Mol, B., Moreno, X., Iacono, C.L., Diez, S., Tello, O., Gómez-Ballesteros, M., Dañobeitia, J.J., 2018. Kinematic analysis of secondary faults within a distributed shear-zone reveals fault linkage and increased seismic hazard. *Marine Geology* 399, 23–33.
<https://doi.org/10.1016/j.margeo.2018.02.002>

- Pérez-Belzuz, F., Alonso, B., Ercilla, G., 1997. History of mud diapirism and trigger mechanisms in the Western Alboran Sea. *Tectonophysics, Structural Controls on Sedimentary Basin Formation* 282, 399–422. [https://doi.org/10.1016/S0040-1951\(97\)00226-6](https://doi.org/10.1016/S0040-1951(97)00226-6)
- Platt, J.P., Whitehouse, M.J., Kelley, S.P., Carter, A., Hollick, L., 2003. Simultaneous extensional exhumation across the Alboran Basin: Implications for the causes of late orogenic extension. *Geology* 31, 251. [https://doi.org/10.1130/0091-7613\(2003\)031<0251:SEEATA>2.0.CO;2](https://doi.org/10.1130/0091-7613(2003)031<0251:SEEATA>2.0.CO;2)
- Principaud, M., Mulder, T., Gillet, H., Borgomano, J., 2015. Large-scale carbonate submarine mass-wasting along the northwestern slope of the Great Bahama Bank (Bahamas): Morphology, architecture, and mechanisms. *Sedimentary Geology, Carbonate slopes and gravity deposits* 317, 27–42. <https://doi.org/10.1016/j.sedgeo.2014.10.008>
- Rashid, H., MacKillop, K., Sherwin, J., Piper, D.J.W., Marche, B., Vermooten, M., 2017. Slope instability on a shallow contourite-dominated continental margin, southeastern Grand Banks, eastern Canada. *Marine Geology, Advancements in Understanding Deep-Sea Clastic Sedimentation Processes* 393, 203–215. <https://doi.org/10.1016/j.margeo.2017.01.001>
- Rebesco, M., 2005. SEDIMENTARY ENVIRONMENTS | Contourites, in: Selley, R.C., Cocks, L.R.M., Plimer, I.R. (Eds.), *Encyclopedia of Geology*. Elsevier, Oxford, pp. 513–527. <https://doi.org/10.1016/B0-12-369396-9/00497-4>
- Rebesco, M., Camerlenghi, A., 2008. Contourites. M. Rebesco, A. Camerlenghi (Eds.), *Developments in Sedimentology*, 60, Elsevier, Amsterdam (2008).
- Rebesco, M., Hernández-Molina, F.J., Van Rooij, D., Wählin, A., 2014. Contourites and associated sediments controlled by deep-water circulation processes: state-of-the-art and future considerations. *Marine Geology* 352, 111–154.
- Riboulot, V., Cattaneo, A., Sultan, N., Garziglia, S., Ker, S., Imbert, P., Voisset, M., 2013. Sea-level change and free gas occurrence influencing a submarine landslide and pockmark formation and distribution in deepwater Nigeria. *Earth and Planetary Science Letters* 375, 78–91. <https://doi.org/10.1016/j.epsl.2013.05.013>
- Rodríguez, M., Maleuvre, C., Jollivet-Castelot, M., d'Acremont, E., Rabaute, A., Lafosse, M., Ercilla, G., Vázquez, J.-T., Alonso, B., Ammar, A., Gorini, C., 2017. Tsunamigenic submarine landslides along the Xauen–Tofiño banks in the Alboran Sea (Western Mediterranean Sea). *Geophys J Int* 209, 266–281. <https://doi.org/10.1093/gji/ggx028>
- Rodríguez, C.E., Bommer, J.J., Chandler, R.J., 1999. Earthquake-induced landslides: 1980–1997. *Soil Dynamics and Earthquake Engineering* 18, 325–346. [https://doi.org/10.1016/S0267-7261\(99\)00012-3](https://doi.org/10.1016/S0267-7261(99)00012-3)
- Rohling, E.J., Foster, G.L., Grant, K.M., Marino, G., Roberts, A.P., Tamisiea, M.E., Williams, F., 2014. Sea-level and deep-sea-temperature variability over the past 5.3 million years. *Nature* 508, 477–482. <https://doi.org/10.1038/nature13230>
- Sawyer, D.E., DeVore, J.R., 2015. Elevated shear strength of sediments on active margins: Evidence for seismic strengthening. *Geophys. Res. Lett.* 42. <https://doi.org/10.1002/2015GL066603>
- Somoza, L., Medialdea, T., León, R., Ercilla, G., Vázquez, J.T., Farran, M., Hernández-Molina, J., González, J., Juan, C., Fernández-Puga, M.C., 2012. Structure of mud volcano systems and pockmarks in the region of the Ceuta Contourite Depositional System (Western Alborán Sea). *Marine Geology, Hydrocarbon leakage through focused fluid flow systems in continental margins* 332–334, 4–26. <https://doi.org/10.1016/j.margeo.2012.06.002>
- Spakman, W., Wortel, R., 2004. A tomographic view on Western Mediterranean Geodynamics, in: Cavazza, W., Roure, F., Spakman, W., Stampfli, G.M., Ziegler, P.

- (Eds.), The TRANSMED Atlas, The Mediterranean Region from Crust to Mantle. pp. 31–52.
- Stich, D., J. Batllo, J. Morales, M. Ramon, D. Savka, 2003. Source parameters of the M W = 6.1 1910 Adra earthquake (southern Spain). *Geophysical Journal International* 539–546.
- Stich, D., Mancilla, F. d. L., Baumont, D., Morales, J., 2005. Source analysis of the Mw 6.3 2004 Al Hoceima earthquake (Morocco) using regional apparent source time functions. *Journal of Geophysical Research* 110. <https://doi.org/10.1029/2004JB003366>
- Stich, D., Martín, R., Morales Soto, J., López Comino, J.Á., Mancilla Pérez, F. de L., 2020. Slip Partitioning in the 2016 Alboran Sea Earthquake Sequence (Western Mediterranean). <https://doi.org/10.3389/feart.2020.587356>
- Stirling, M., Goded, T., Berryman, K., Litchfield, N., 2013. Selection of Earthquake Scaling Relationships for Seismic-Hazard Analysis. *Bulletin of the Seismological Society of America* 103, 2993–3011. <https://doi.org/10.1785/0120130052>
- Sultan, N., Cochonat, P., Canals, M., Cattaneo, A., Dennielou, B., Haflidason, H., Laberg, J.S., Long, D., Mienert, J., Trincardi, F., Urgeles, R., Vorren, T.O., Wilson, C., 2004. Triggering mechanisms of slope instability processes and sediment failures on continental margins: a geotechnical approach. *Marine Geology, COSTA - Continental Slope Stability* 213, 291–321. <https://doi.org/10.1016/j.margeo.2004.10.011>
- Tappin, D.R., Watts, P., McMurtry, G.M., Lafoy, Y., Matsumoto, T., 2001. The Sissano, Papua New Guinea tsunami of July 1998 — offshore evidence on the source mechanism. *Marine Geology* 175, 1–23. [https://doi.org/10.1016/S0025-3227\(01\)00131-1](https://doi.org/10.1016/S0025-3227(01)00131-1)
- Taylor, D.W., 1948. *Fundamentals of Soil Mechanics*. Soil Science 66, 161. ten Brink, U.S., Andrews, B.D., Miller, N.C., 2016. Seismicity and sedimentation rate effects on submarine slope stability. *Geology* 44, 563–566. <https://doi.org/10.1130/G37866.1>
- Triantafyllou, I., Gogou, M., Mavroulis, S., Lekkas, E., Papadopoulos, G.A., Thravalos, M., 2021. The Tsunami Caused by the 30 October 2020 Samos (Aegean Sea) Mw7. 0 Earthquake: Hydrodynamic Features, Source Properties and Impact Assessment from Post-Event Field Survey and Video Records. *Journal of Marine Science and Engineering* 9, 68.
- Urgeles, R., Camerlenghi, A., 2013. Submarine landslides of the Mediterranean Sea: Trigger mechanisms, dynamics, and frequency-magnitude distribution. *Journal of Geophysical Research: Earth Surface* 118, 2600–2618. <https://doi.org/10.1002/2013JF002720>
- Urlaub, M., Talling, P.J., Zervos, A., Masson, D., 2015. What causes large submarine landslides on low gradient (<2°) continental slopes with slow (~0.15 m/kyr) sediment accumulation? *Journal of Geophysical Research: Solid Earth* 120, 6722–6739. <https://doi.org/10.1002/2015JB012347>
- Valensise, G., Pantosti, D., 1992. A 125 Kyr-long geological record of seismic source repeatability: the Messina Straits (southern Italy) and the 1908 earthquake (Ms 7.1/2). *Terra Nova* 4, 472–483. <https://doi.org/10.1111/j.1365-3121.1992.tb00583.x>
- Wesnowsky, S.G., Scholz, C.H., Shimazaki, K., Matsuda, T., 1983. Earthquake frequency distribution and the mechanics of faulting. *Journal of Geophysical Research: Solid Earth* 88, 9331–9340. <https://doi.org/10.1029/JB088iB11p09331>
- Yen, Y.-T., Ma, K.-F., 2011. Source-Scaling Relationship for M 4.6–8.9 Earthquakes, Specifically for Earthquakes in the Collision Zone of Taiwan. *Bulletin of the Seismological Society of America* 101, 464–481. <https://doi.org/10.1785/0120100046>

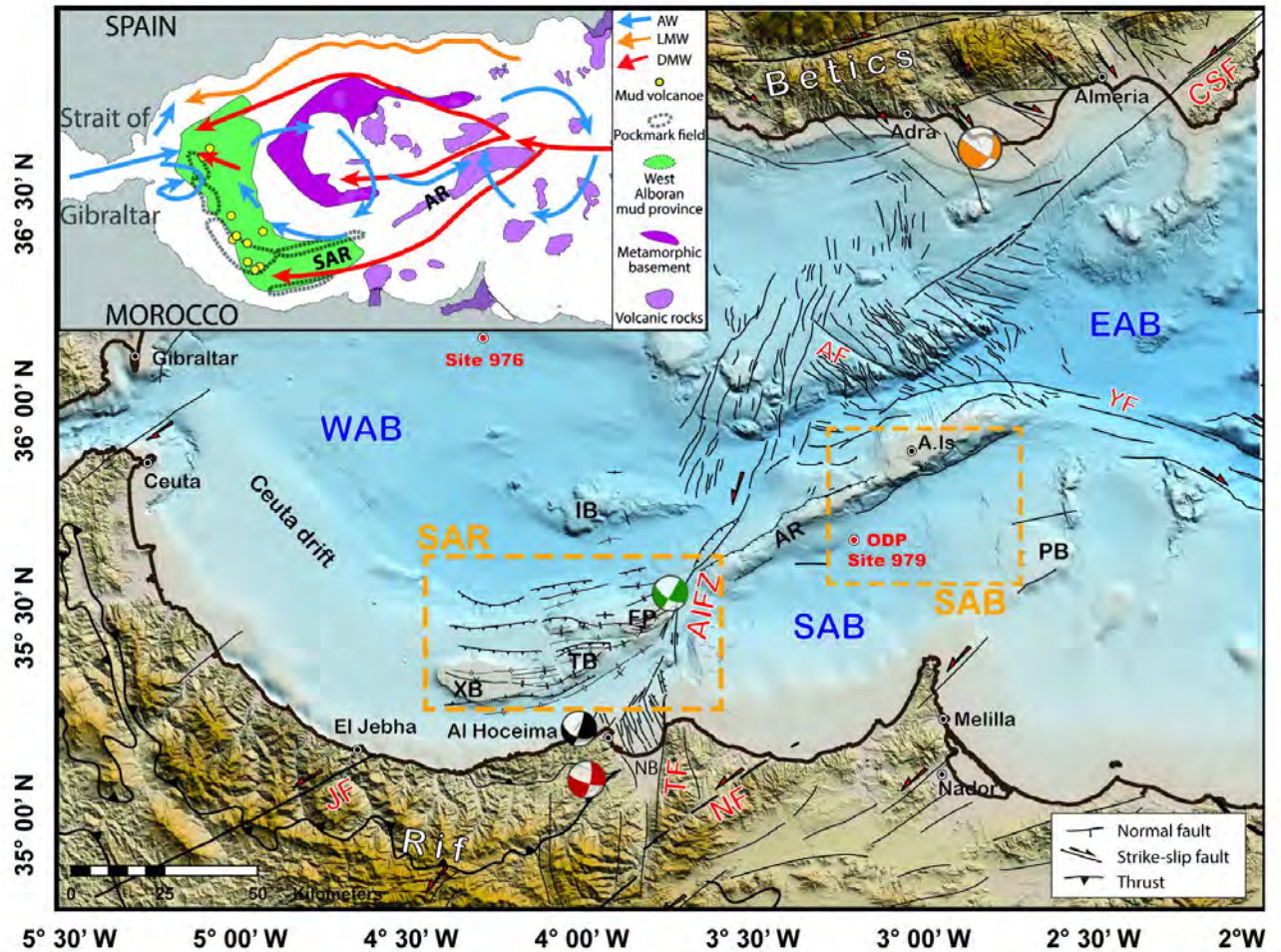


Figure 1: Bathymetric map of the Alboran Sea showing the structural features of the area. Shaded bathymetry from compilation of ISTEP and CSIC multibeam cruises with GEBCO 2014 database, topography from SRTM database. Focal mechanism in black: 1994 main shock (El Alami et al., 1998; Biggs et al., 2006). Focal mechanism in red: 2004 main shock (van der Woerd et al., 2014). Focal mechanism in green: 2016 main shock (Kariche et al., 2017; Medina and Cherkaoui, 2017). Focal mechanism in orange: Location and moment tensor solution obtained for the 1910 Adra Earthquake from Stich et al. (2003). AF, Averroes Fault; AIFZ, Al Idrissi Fault Zone; A.Is, Alboran Island; AR, Alboran Ridge (Alboran ridge thrust front, ARTF); CSF, Carboneras Serrata Fault; EAB, East Alboran Basin; FP, Francesc Pagès Seamount; IB, Ibn-Batouta Bank; JF, Jebha Fault; NB, Nekor Basin; NF, Nekor Fault; PB, Pytheas Bank; SAB, South Alboran Basin; SAR, South Alboran Ridge; TB, Tofiño Bank; WAB, West Alboran Basin; XB, Xauen Bank; YF, Yusuf Fault. Orange dashed areas SAB and SAR correspond to the two key sites of this study (South Alboran Basin and South Alboran Ridge respectively). Offshore structural features from Estrada et al. (2017); d'Acremont et al. (2020). Inset: water currents between Mediterranean Sea and Atlantic Ocean and main features of the basement. The arrows representing water masses are from Ercilla et al. (2019); AW, Atlantic Water; LMW, Light Mediterranean intermediate Water; DMW, Dense Mediterranean Water.

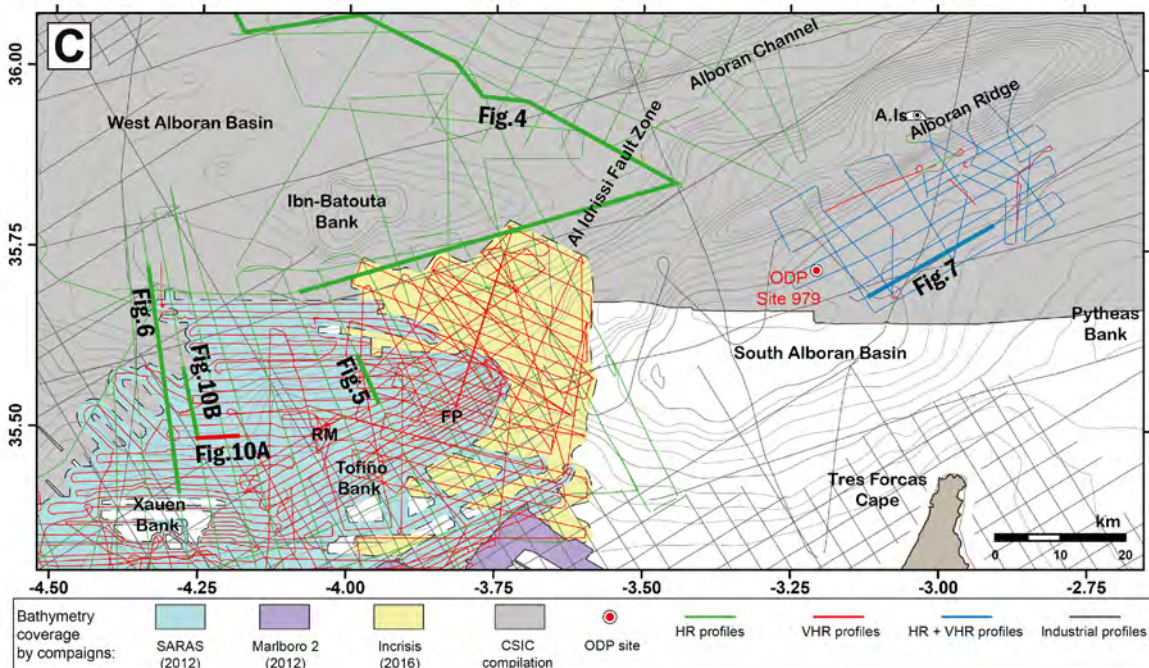
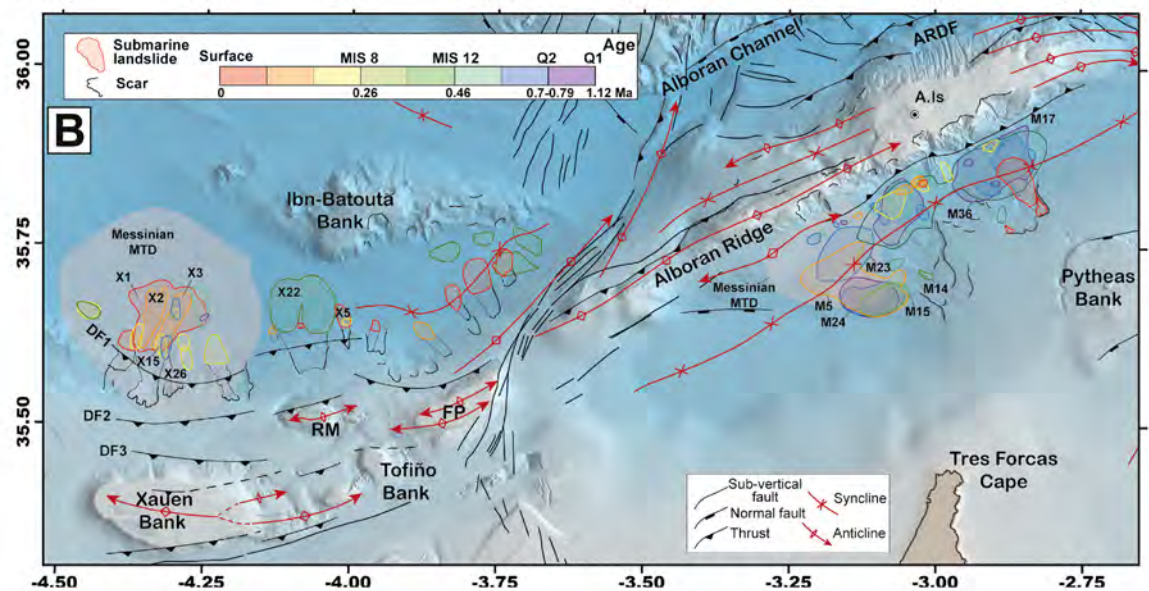
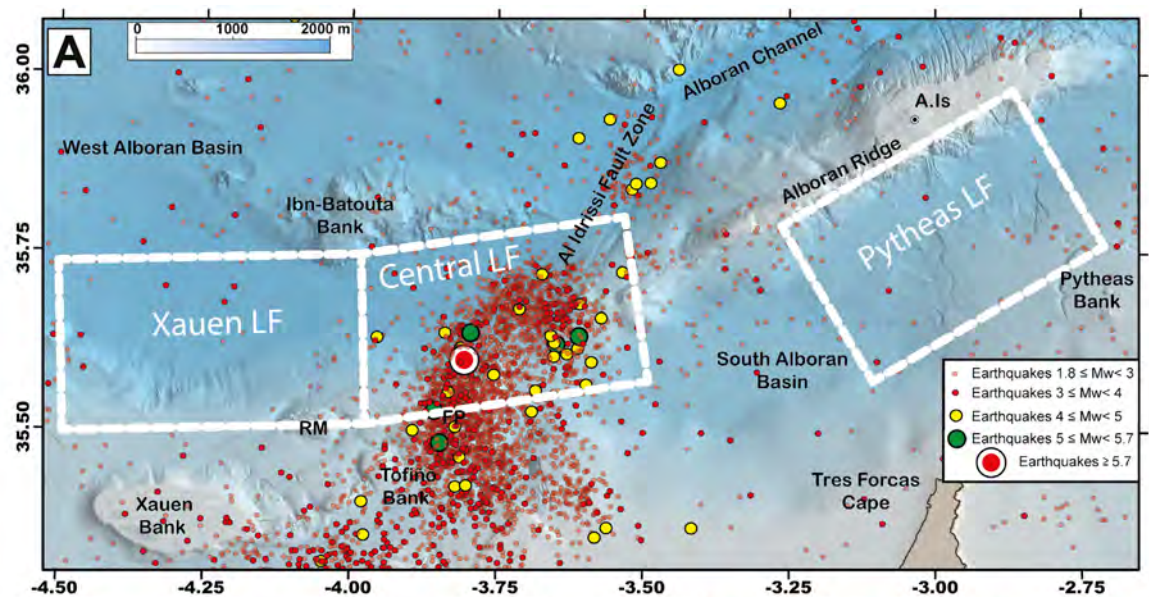


Figure 2: (A) Bathymetric and seismic epicentral map. Epicentres of the earthquakes recorded between 1964 and 2020 (Spanish Instituto Geografico Nacional (IGN) database). Landslide field location used in the text and Figure 9 (Xauen, Central and Pytheas) is represented by the white line. (B) Structural map (from d'Acremont et al. 2020; Lafosse et al. 2020) with the distribution of the submarine landslides from this study. Xx and Mx correspond to the code names of the MTDs described in this paper (see Appendix). DF1, DF2, DF3, deformation front highlighted by blind thrusts from d'Acremont et al. 2020. ARDF, Alboran Ridge Deformation Front from Martinez-Garcia et al. 2017. A.Is, Alboran Island; FP, Francesc Pagès Seamount; RM, Ramon Margalef High. (C) Swath bathymetric and seismic reflection coverage of the study area, from CONTOURIBER (2010), Marlboro-1 (2011), Marlboro-2 (2012), SARAS (2012), MONTERA (2012), and INCRISIS (2016) projects and the Fishing General Secretary (Spanish Government) (HR: high resolution; VHR: very high resolution). Thick lines correspond to seismic reflection profiles shown in this paper with the figure number.

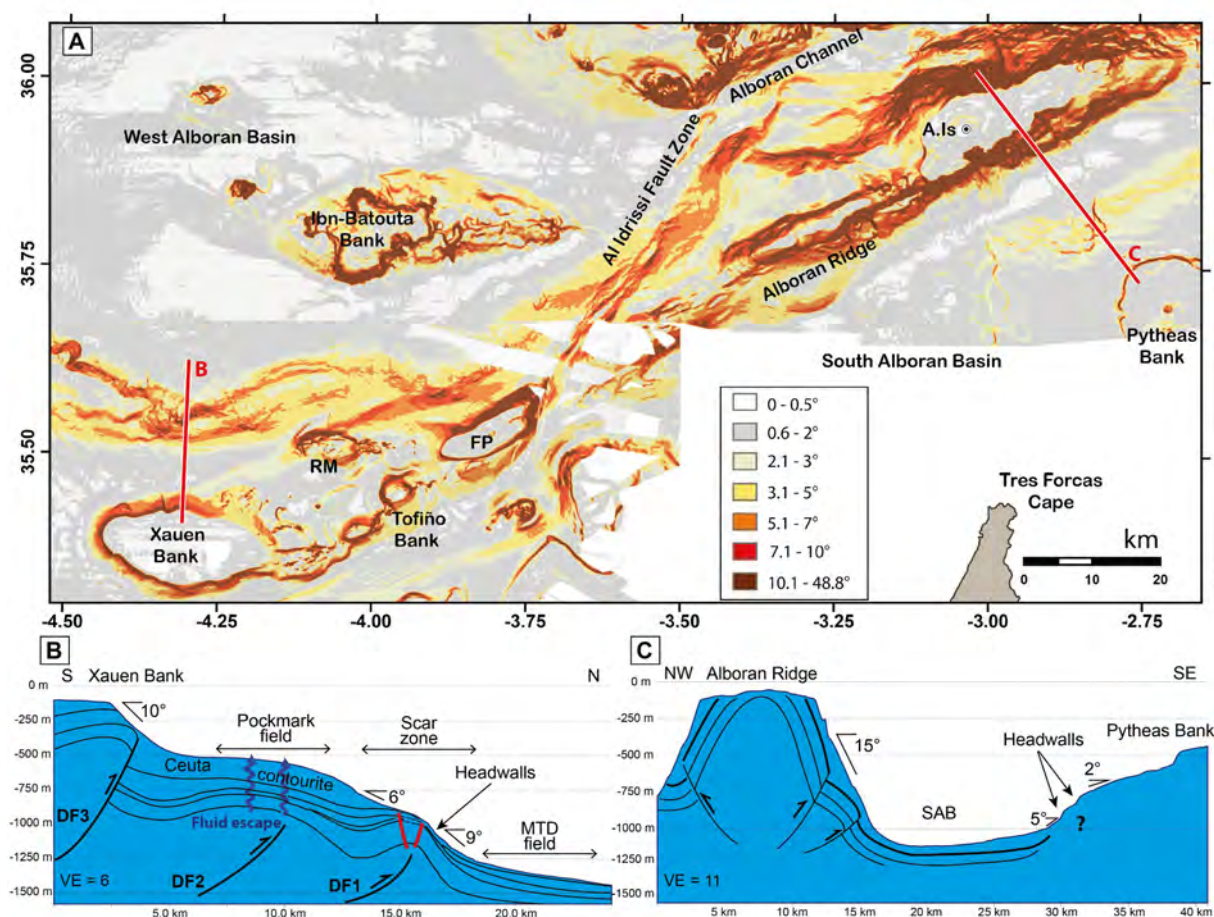


Figure 3: (A) Slope map of Southern Alboran Sea and slope failures. A.Is, Alboran Island; FP, Francesc Pagès Seamount; RM, Ramon Margalef High. (B)(C) Bathymetric profiles located in (A) with structural shape, slope values (from d'Acremont et al. 2020). VE, vertical exaggeration. DF1, DF2, DF3, deformation front highlighted by blind thrusts. MTD, Mass Transport Deposit.

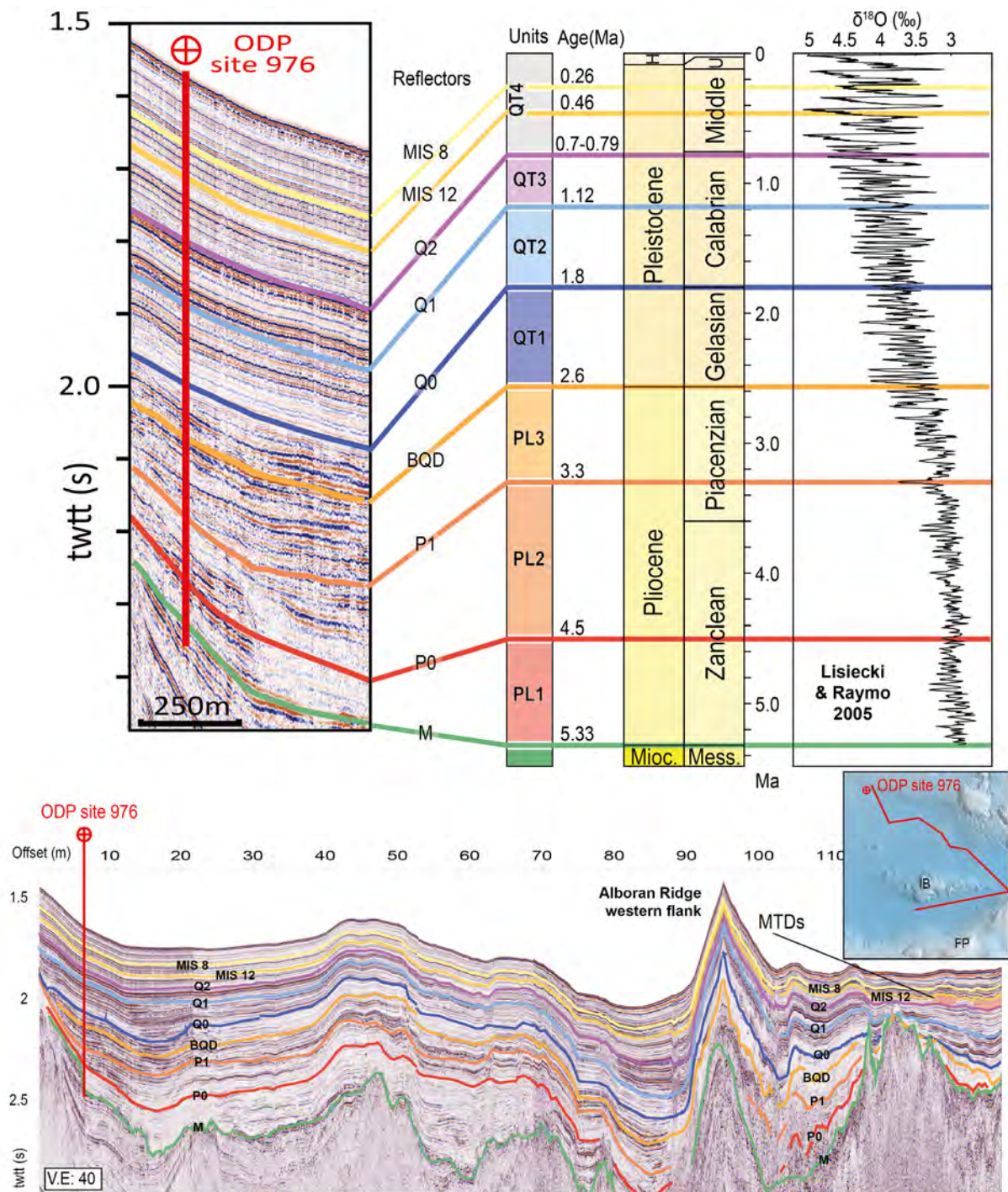


Figure 4: Chronostratigraphic units and seismic horizons using ODP sites 976 (Units from Juan et al., 2016). Benthic $\delta^{18}O$ curve from Lisiecki and Raymo (2005). Composite seismic reflection profile used to follow the chronostratigraphic units from the ODP site 976 to the study area. IB, Ibn Batouta; FP, Francesc Pagès, Mioc., Miocene; Mess., Messinian; H, Holocene; U upper. MIS 12 and MIS 8 represent Marine Isotope stages, we have used this term as the name of the reflectors.

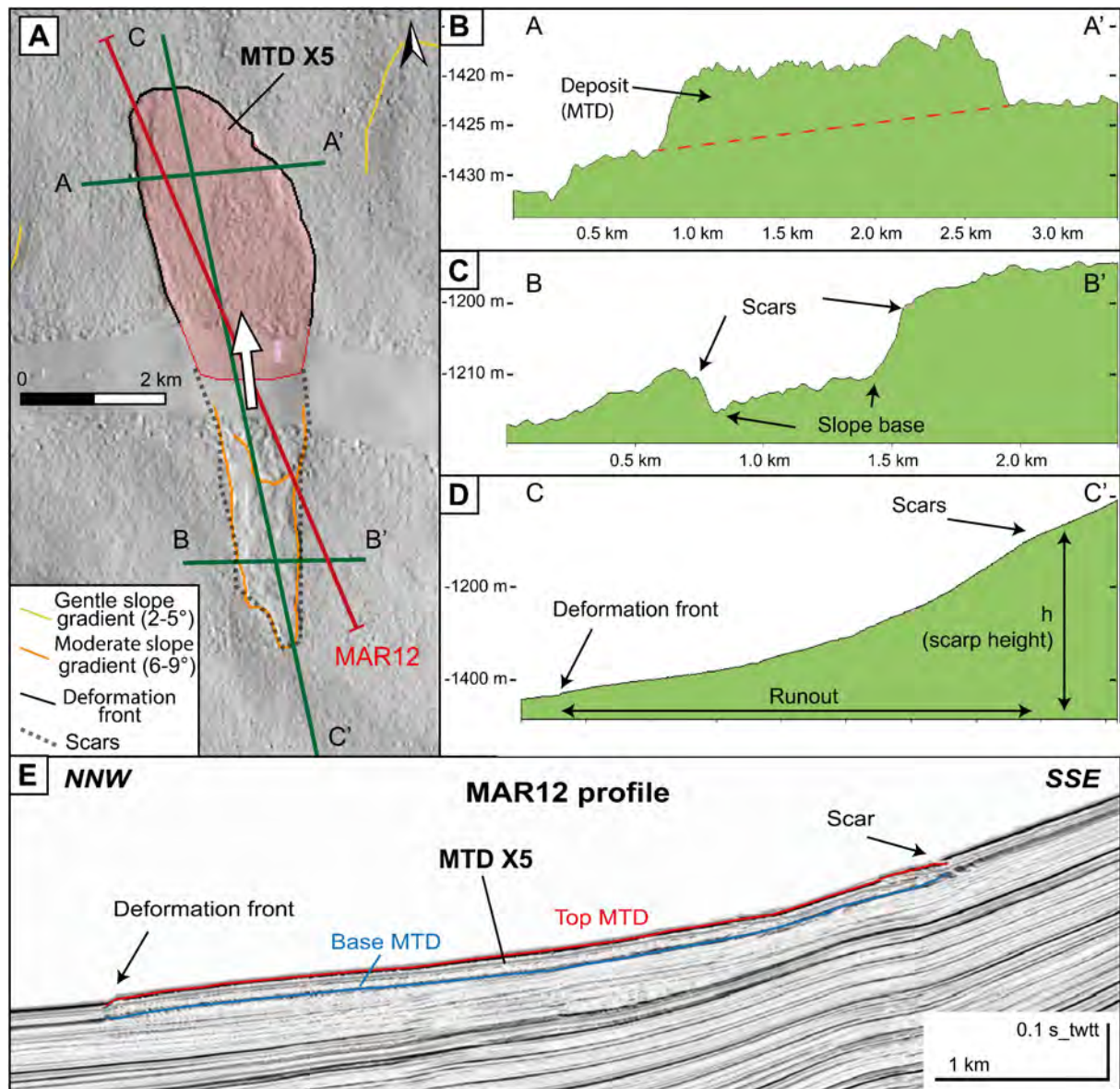


Figure 5 : Characterization of a submarine landslide using bathymetry (A), slope profiles (B, C, D) and seismic reflection profile (E): example of MTD X5 along the Xauen Bank northern flank. The white arrow indicates direction of transport of the submarine landslide.

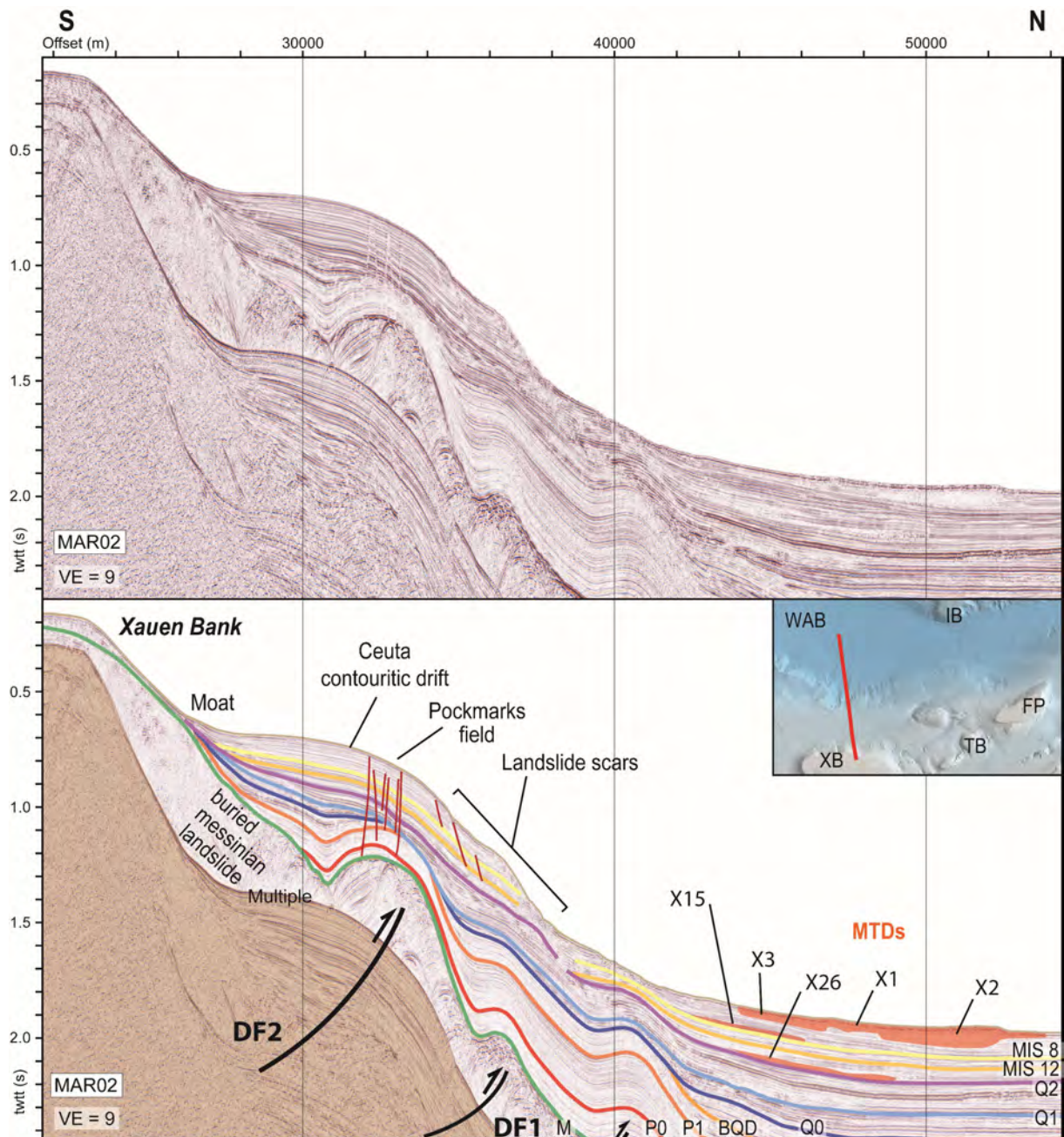


Figure 6 : High-resolution profile from Marlboro 1 campaign (MAR02), between the Xauen Bank (XB) and the southern WAB. It shows localization of landslide scars along slopes north to the Xauen Bank, where slope gradient is affected by contouritic sedimentation (Ceuta contourite drift) and northward vergence thrusts (DF1, DF2) as well as mass transport deposits (Xx mapped in Figure 2B). TB Tofiño Bank, FP Francesc Pagès Seamount, IB Ibn Batouta seamount. P0, P1, BQD, Q0, Q1, Q2, MIS12 and MIS8 refer to seismic reflectors defined in figure 4.

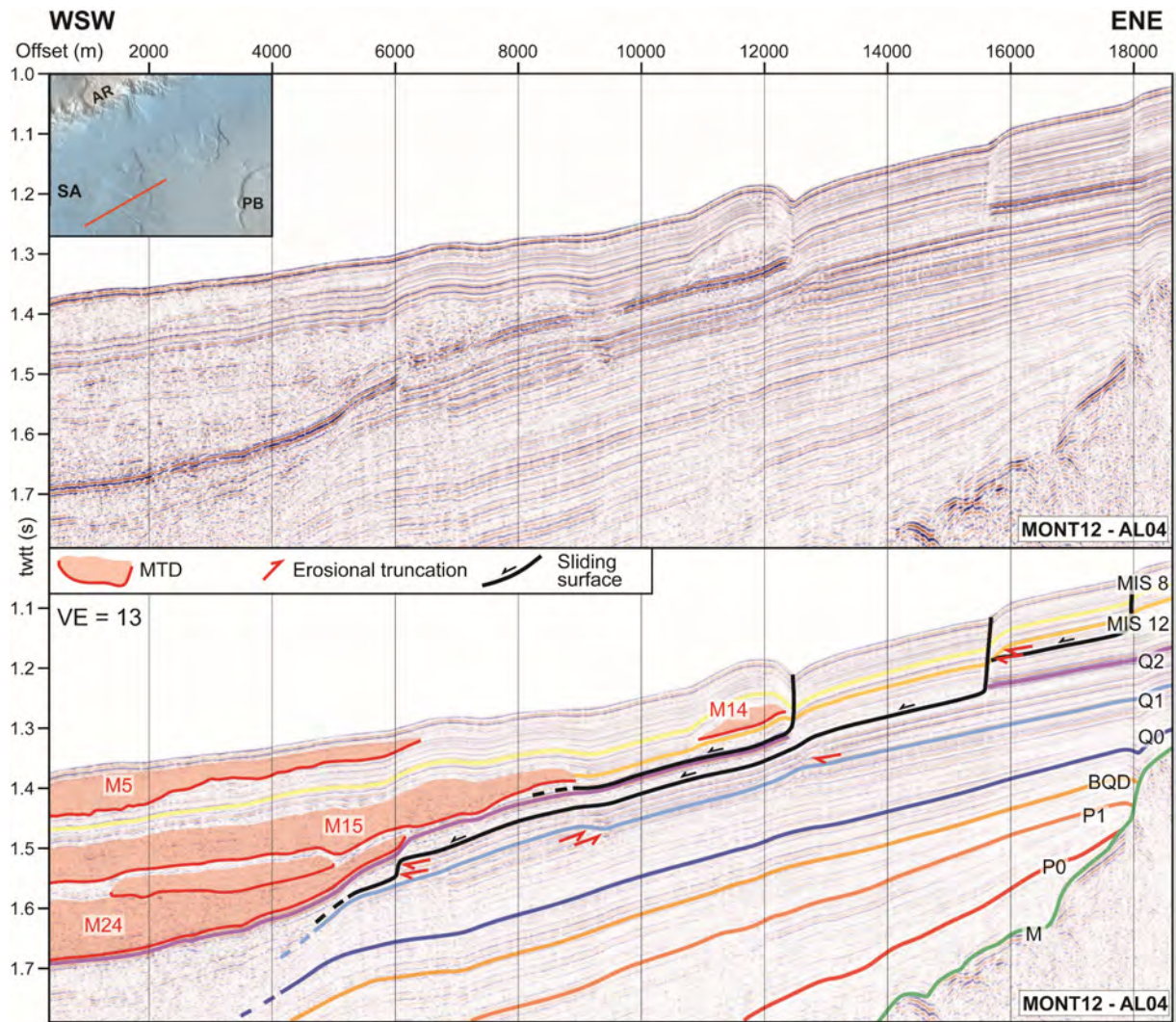


Figure 7: High-resolution profile from MONTERA campaign (AL04), in the southern SAB. It highlights buried MTDs downward the slope and three decollement levels above the Q1 reflector. Mx Mass transport deposits represented in map Figure 2B. AR Alboran Ridge, PB Pytheas Bank, M, P0, P1, BQD, Q0, xx refer to seismic reflectors defined in figure 4.

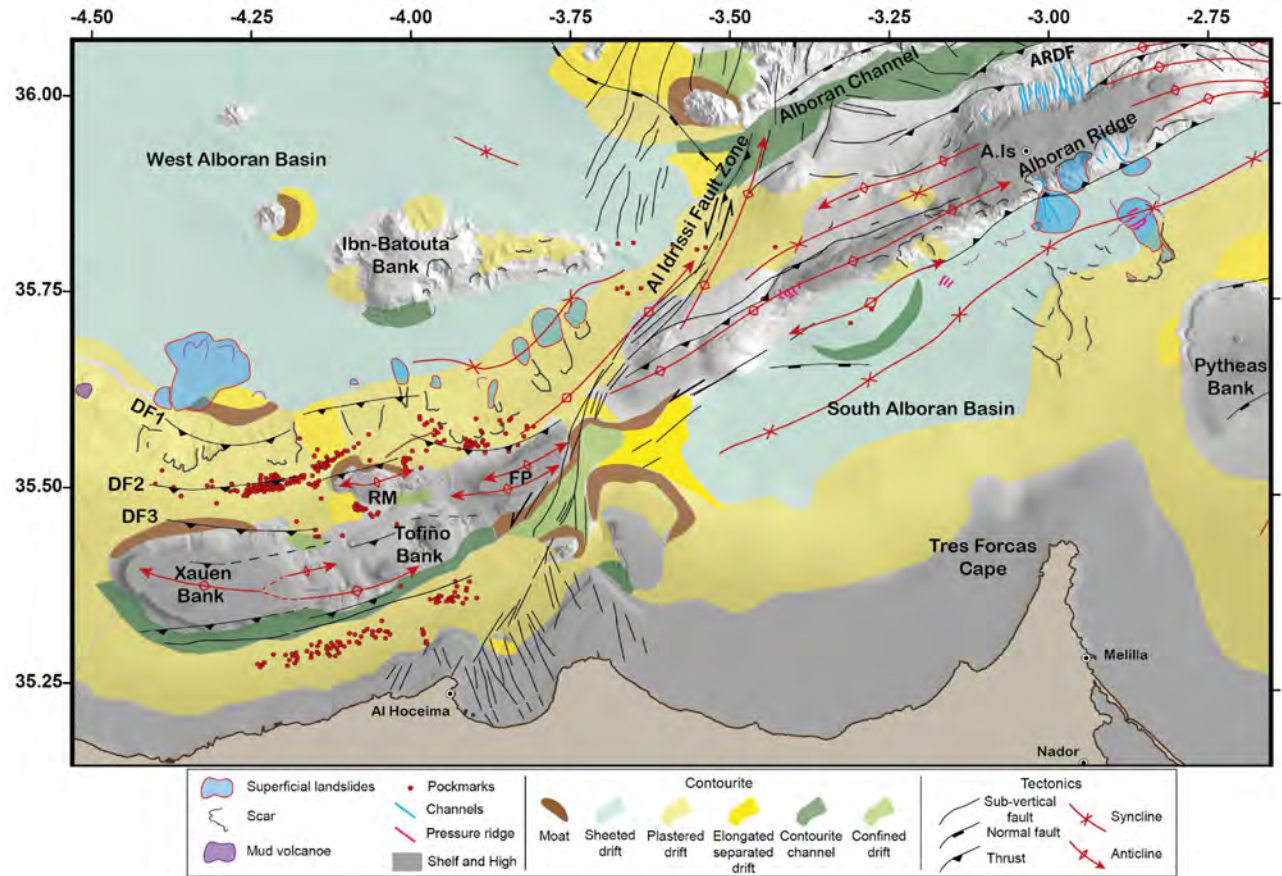


Figure 8: Morpho-structural map of the study area. Contourite deposits from Ercilla et al. 2019, structural features from d'Acremont et al. (2020) and Lafosse et al. (2020). A.Is, Alboran Island; BBFZ, Boussekkour-Bokkoya Fault Zone; FP, Francesc Pagès Seamount; RM, Ramon Margalef High. DF1, DF2, DF3, deformation front highlighted by blind thrusts.

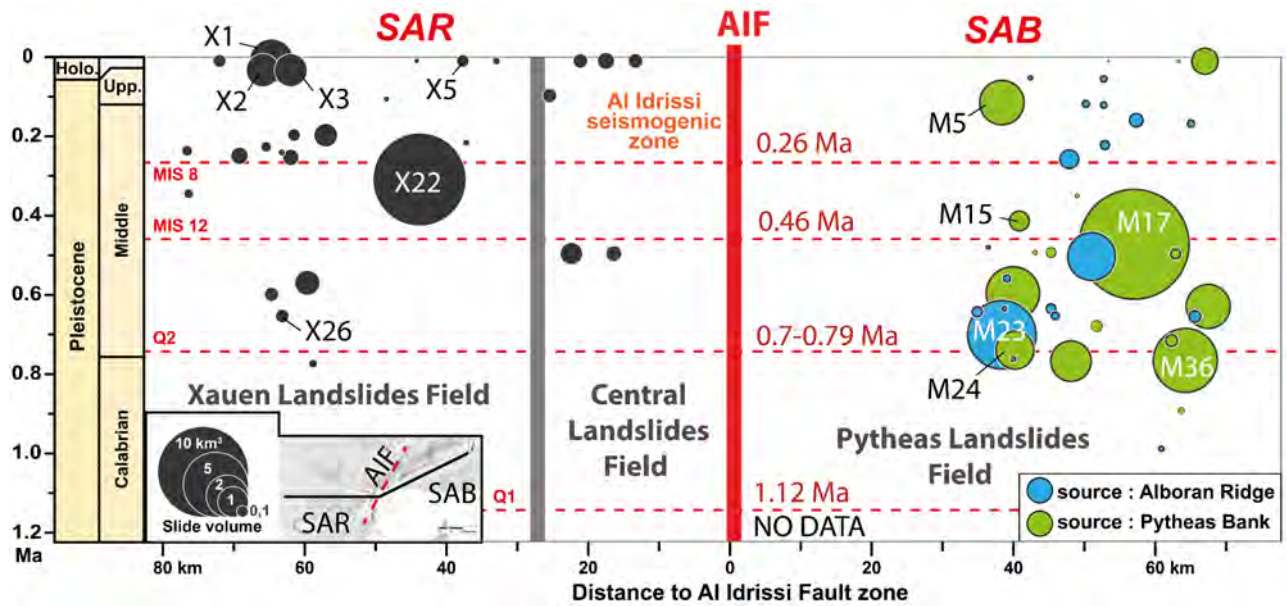


Figure 9: Distribution of MTDs observed and quantified in the southern part of the Alboran Sea, west and east of the AIFZ. The three landslide fields are localized in the Figure 2A: Xauen landslides field north to the Xauen and Tofiño Banks; Central landslides field north of the Francesc Pagès Seamount; Pytheas landslides field between the Alboran Ridge and the Pytheas bank. The MTDs are represented according to their age, volumes and for those in the east, their sources. See Appendix A1 and A2 for MTD characteristics. Xx and Mx correspond to the code names of the MTDs described and shown in Figure 2B.

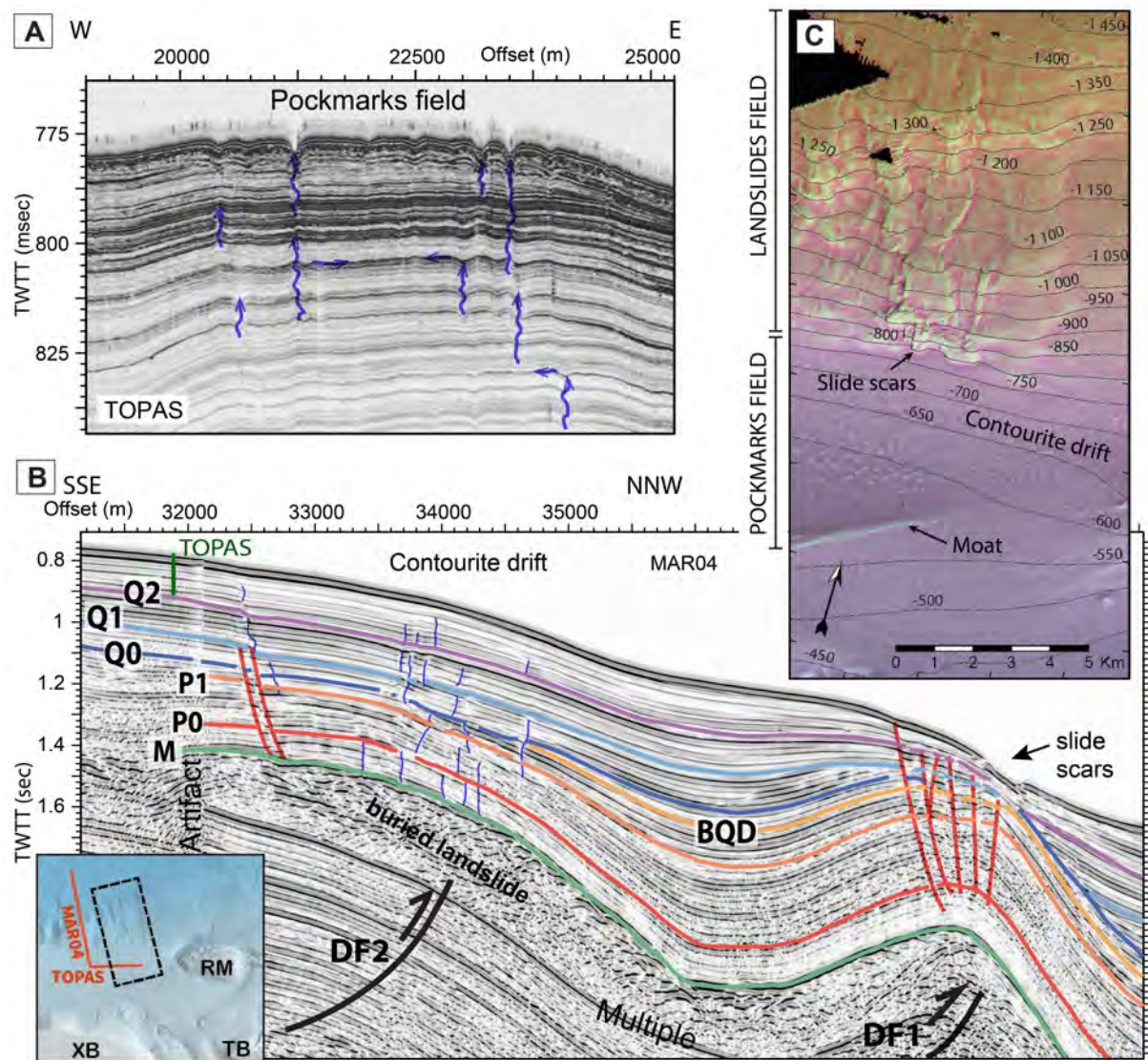


Figure 10: Fluid escape and compactional fault features through contourite drift in the SAR region (north Xauen Bank). A. Sub-seabed expression of fluid escapes and pockmarks on ultra-high resolution seismic reflection data (TOPAS). Location in B. B. High-resolution seismic reflection data showing the deformation below the contourite drift, associated to faults and fluid escapes. The normal faults here are interpreted as due to fold extrados extension from blind thrusts. Inset: in red location of MAR04 and TOPAS profiles, black rectangle corresponds to bathymetric zoom C. C. Seabed expression of pockmarks and landslide scar. Bathymetric data with contours every 50m. XB, Xauen Bank; TB, Tofino Bank; RM, Ramon Margalef Seamount.

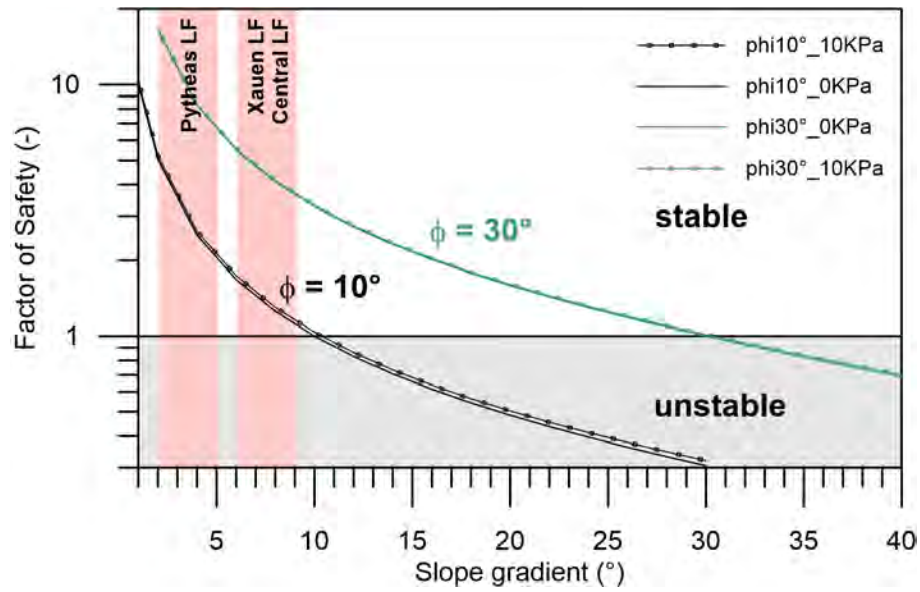


Figure 11 : Factor of safety calculations based on the infinite slope approach (FOSIS) illustrating that according to the Mohr-Coulomb criteria, the minimum slope angle required to trigger a failure is the friction angle. Calculations for three values of cohesions illustrates the restricted effects on the stability. Area of the three landslide fields (LF) according to their slope gradients are represented in pink. ϕ friction angle (ϕ); Cohesion (KPa).

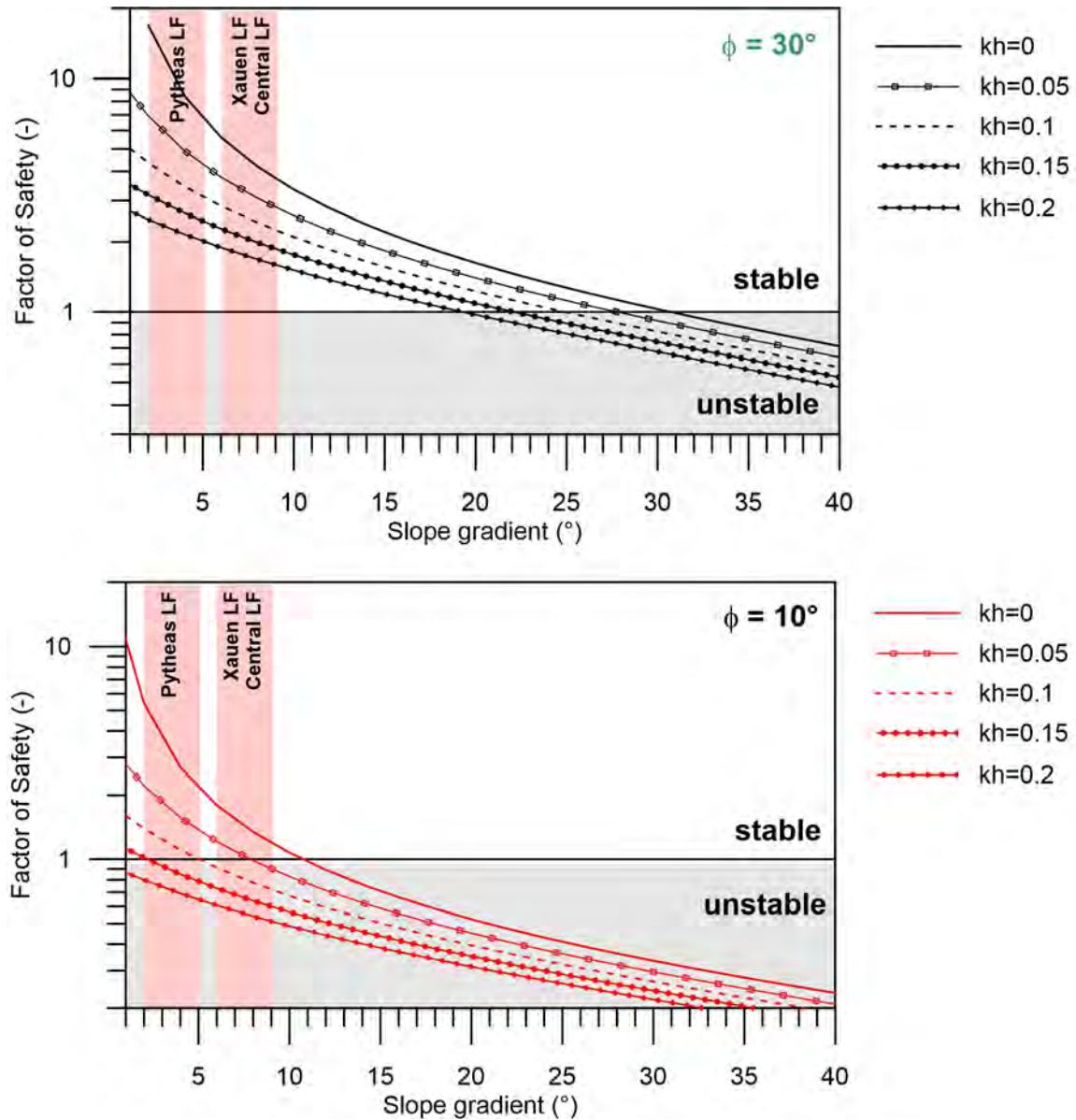


Figure 12: Factor of safety calculations based on the pseudostatic approach (FOSPS) for seismic coefficients kh from 0 to 0.2. Top: scenario of sediments with a friction angle of 30° . Bottom: scenario of sediments with a friction angle of 10° . Instability may be attained for the Xauen and Central Landslide Fields (LF) if $kh > 0.05$, and for the Pytheas LF $kh > 0.1$. ϕ friction angle; kh pseudostatic seismic coefficient.

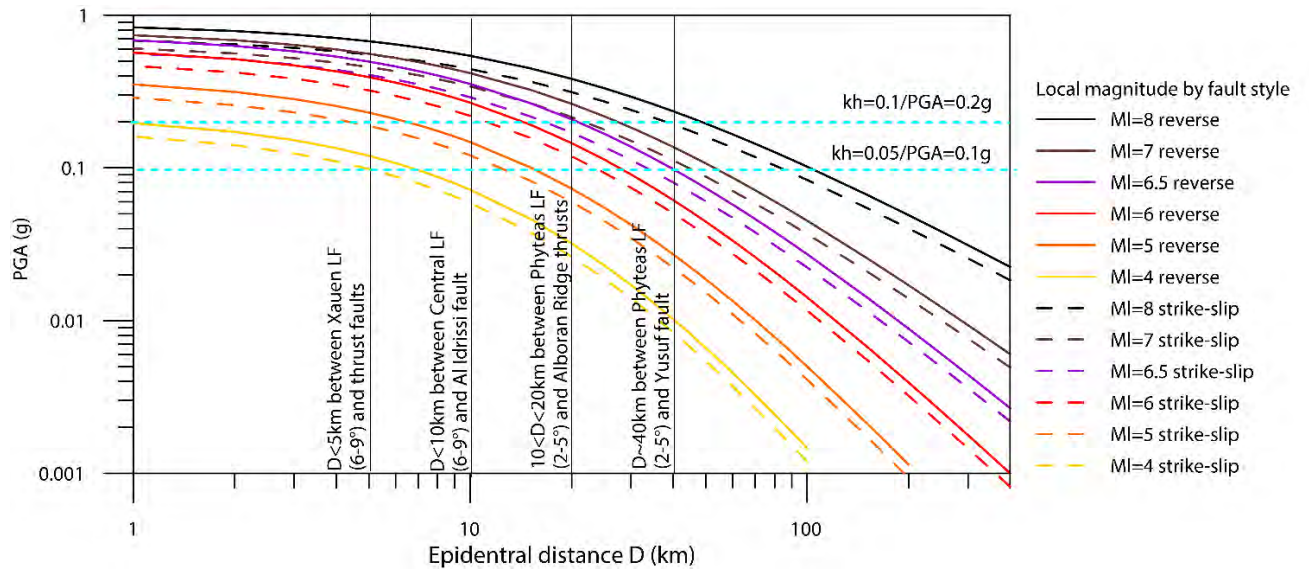


Figure 13: Peak Ground Accelerations (PGA) obtained for reverse and strike-slip earthquakes as function of the epicentral distance. kh pseudostatic seismic coefficient. MI earthquake magnitude. D - distance between the landslide field (scar features) and the closest tectonic structure (See Appendix A6 for details).